Simulating 3D Orthotropic Cardiac Electromechanics Incorporating Stress-Assisted Diffusion

Adrienne Propp

Corpus Christi College

University of Oxford

A thesis submitted for the degree of

Master of Science in Mathematical Modelling and Scientific Computing

August 2018

Acknowledgements

First and foremost, I would like to thank my supervisor, Dr. Ricardo Ruiz Baier, for enthusiastically including me in his research and guiding me through a most engaging and fulfilling dissertation. I always left our meetings feeling energized, motivated, and confident. It was truly a pleasure and an honor to work with him.

I would also like to thank Dr. Kathryn Gillow for her time and effort. We were lucky to have someone so dedicated to our well-being and success. I also extend a big thank you to our other professors, the faculty, and the other students of the Mathematical Institute for fostering an inspiring academic environment.

I can never express enough gratitude to my parents. Even from thousands of miles away, they offer me support when I need it and laughs always.

Finally, thank you to everyone who made this year so special — the MMSC cohort, the Corpus Christi MCR, my flatmates, the Oxford University Mountaineering Society, the Corpus-Pembroke Women's Football Club, my friends from undergraduate, and all the other people I had the pleasure to meet. This year was everything I wanted it to be, and for this I am deeply grateful.

To my coursemates, remember: "we derive together, we die together!"

Abstract

In this dissertation, we advance a theoretical framework for modeling the electromechanics of the heart tissue. The set of governing equations describes both mechanical deformation and electrophysiology, and accounts for their interaction. Our mechanical model is based on foundations of nonlinear continuum mechanics, following an orthotropic exponential constitutive law for the passive tissue deformation. We consider both the viscoelastic case and the more traditional but idealized hyperelastic case. We couple this mechanical system with a four-variable phenomenological model for human ventricular action potential. We achieve electromechanical coupling through both active tension, encoded in models of active strain and active stress, and stress-assisted diffusion. The inclusion of stress-assisted diffusion, in particular, is a novel aspect of our model that has not yet been incorporated into an active stress framework or viscoelastic mechanical model.

We first implement our model in 2D using a mixed-primal finite element scheme. We perform computational tests to investigate the effects of our model's parameters, as well as the effects of viscosity and stress-assisted diffusion. We then extend the model to 3D, although this requires some adaptation of our original formulation to yield anatomically accurate results. We conclude by proposing several possible extensions to our model.

Contents

List of Figures

Chapter 1

Introduction

1.1 Motivation

Cardiovascular disease is the leading cause of death worldwide [1], despite the extensive research that has made the heart one of the most well-studied organs [61]. The global community is committed to fighting this pandemic; institutions like the World Health Organization have established action plans to increase awareness of, monitor, and assess its severity [1]. In order to effectively combat cardiovascular disease, however, we need a robust scientific understanding of the workings of the heart and the nature of such health conditions.

Recent progress in the field is encouraging. The concept of patient-specific treatments is no longer a distant dream, but a conceivable reality and the topic of ongoing research [13, 27, 41]. However, a major obstacle is our incomplete knowledge about the relationship between processes at the cellular and subcellular level, and the performance of the organ as a whole [5]. Indeed, a great deal of treatment is still based on trial-and-error experimentation rather than true scientific understanding of the changes responsible for the onset and progression of disease [26]. Several treatments, such as resynchronization therapy and antiarrhythmic medications, for example, are known to be ineffective or even exacerbate pathological conditions in some patients, for reasons that are not yet well understood [8, 32, 69].

An obstacle to deep understanding of cardiac function is the difficulty of acquiring sufficiently detailed data [40]. Until recently, there were no experimental techniques capable of recording 3D cardiac activity with high enough spatio-temporal resolution to provide the required level of information [65]. A recent study by Christoph et al. [18] is one of the first, having succeeded in using optical mapping to assess electromechanical waves.

Computational models have thus been critical in allowing for extensive study of the heart even without sufficient data. The development of complex multi-scale and multi-physics models, accompanied by advances in simulation and imaging techniques, has enabled researchers to investigate the many different aspects of cardiac function and disease [40]. The hope is that the knowledge gained from these models can contribute to new and improved treatment methods [26]. In this dissertation, we seek to contribute to the current state of computational cardiac modeling.

The heart is an incredibly complex organ, with subprocesses occurring and interacting with one another at different spatial and temporal scales (see Figure 1.1) [67]. The scientific community has generally approached the formidable task of modeling cardiac function by addressing these subprocesses separately, with the intention of later combining them into a comprehensive whole-heart model [64]. Thus most cardiac modeling studies to date have focused on either the mechanical or electrochemical aspects, and these fields have historically advanced almost independently [5]. Investigations of cardiac mechanics can be traced back to Woods' 1892 model for stress in the heart wall [13], though most of our understanding of the heart's geometry and the importance of its nonlinear mechanical properties did not emerge until
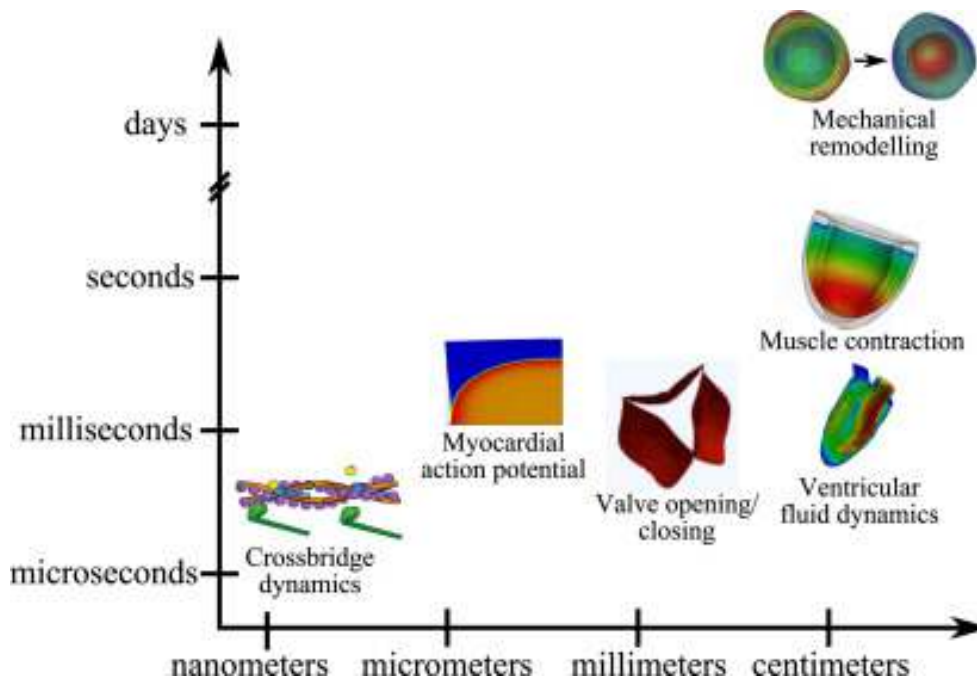

Figure 1.1: Spatial and temporal scales of processes contributing to heart function. Models of heart function typically incorporate some combination of these subprocesses. Our model focuses on myocardial action potential and muscle contraction. Figure taken from [52].

the 1970s. Cardiac electrophysiology owes much of its progress to the Hodgkin and Huxley models of the 1950s, which paved the way for detailed models of electrical activity by focusing on the underlying physiology [61].

While the literature is extensive with respect to both areas of cardiac modeling, there has been comparatively little work done to merge the two [5, 48]. In particular, *mechanoelectrical feedback* (MEF), which accounts for the multi-scale interactions through which mechanical deformation affects electrical properties, is often omitted [45]. There is a parallel trend in the experimental realm — a great deal of available data has been acquired by suppressing mechanical deformation [16], thus limiting the extent to which we can learn about its effect on electrical properties.

This independence of the mechanical and electrochemical realms of cardiac modeling is problematic. The vast majority of cardiac models have been developed to investigate the mechanisms of cardiac *arrhythmia*, or irregular heartbeat [64]. This type of abnormal electrical activity, which is thought to be associated with *reentrant* electrical waves [45], is extremely dangerous and a major cause of sudden cardiac death [20]. Although there is strong reason to believe that mechanical deformation affects reentrant arrhythmias [48], few studies actually incorporate this [45]. The role of mechanics in arrhythmia is still not completely understood [18], but experiments by Loppini et al. [42] showed that mechanoelectrical feedback plays a major role in electrical activation, and it is also believed to be relevant for many pathological conditions [48]. Consider, for example, *commotio cordis*, in which physical impact to the heart initiates ventricular fibrillation, and *precordial thump*, in which physical impact can stop fibrillation [37].

In recognition of this disconnect, several groups have made a concerted effort to construct more complete models. Recent work has focused on: improving computational methods for coupling mechanics and electrophysiology [5, 14, 62]; incorporating a third field of fluid dynamics to account for the effects of blood flow on cardiac function [67, 68] (see [52] for a recent review); and developing whole-heart, 3D, and patient-specific models [27, 41, 64]. The next step will be to integrate the knowledge gained from these advances in modeling with clinical applications, thereby improving diagnosis, therapy, and prognosis.

1.2   Goals of this Dissertation

The overarching goal of this dissertation is to advance the theoretical framework for modeling orthotropic cardiac electromechanics, incorporating the phenomenon of stress-assisted diffusion. While this study builds upon previous work in the field (most notably Cherubini et al. [16, 17], Loppini et al. [42]), our model contributes several novelties.

A distinguishing feature of our approach is the introduction of the mechanoelectrical feedback (MEF) in the conductivity tensor, through a direct dependence on the Kirchhoff stress; in the literature this is referred to as *stress-assisted diffusion* (SAD). As we have discussed, mechanoelectrical feedback is often omitted from cardiac models. Those that do include MEF generally only account for stretch-activated channels and not SAD. However, recent studies [16, 42] have demonstrated that SAD exerts significant effects in electromechanical models of cardiac function. This dissertation provides further insight into the role of SAD in cardiac electromechanics by investigating its effects in a more advanced model, both in its description of mechanics and electrophysiology.

While both [16, 42] consider only hyperelastic tissue, we also consider the viscoelastic case. Furthermore, our model incorporates a three-field elasticity formulation, motivated by the desire to avoid volumetric locking and to solve directly for variables of interest. In particular, we solve for the Kirchhoff stress, which we use explicitly in our incorporation of SAD. This formulation, which includes a pressure-stabilization term needed in the lowest-order case, is a generalization of the three-field formulation for nearly incompressible hyperelasticity, designed in Chavan et al. [14] using quadrilateral meshes.

We further advance the framework put forth by recent studies by including a more realistic model for ventricular action potential. More precisely, we adopt the Bueno-Orovio et al. [10] human-specific model, which is generally considered to be the minimal model required to accurately reproduce action potential morphologies. Both Loppini et al. [42] and Cherubini et al. [16] investigated SAD using simpler models.

Finally, we implement our model on an idealized 3D geometry, which has not yet been done for models incorporating SAD. In fact, we are not aware of any existing literature that has implemented a viscoelastic and anisotropic model incorporating stress-assisted conductivities in a stress-based formulation, particularly in 3D geometries. Thus, this dissertation contributes a unique framework for studying the effects of SAD.

This dissertation is presented as follows. We conclude this chapter with a brief overview of cardiac function to familiarize the reader with the subject of our work. In Chapter 2, we describe the mathematical models that we use to construct a fully coupled electromechanical model of cardiac function. We discuss the mechanical and electrophysiological components separately, then describe our coupling of the two fields and the extension to 3D. In Chapter 3, we outline the numerical implementation of our model. Chapter 4 provides an overview of our results, which we discuss in Chapter 5, along with possible extensions of our model.

1.3 Overview of the Cardiac Cycle and Physiology

We now provide a brief overview of the cardiac cycle. This chapter is not intended to be a comprehensive description; instead, we strive to highlight details that are important from a modeling perspective, lending insight into the assumptions and decisions we make in constructing our model.

It is important to consider features of the heart at both a macroscopic and microscopic level. Macroscopically, the heart is comprised of four parts: the left and right atria and the left and right ventricles. Both sides of the heart follow the same overall cycle, though the right side of the heart pumps deoxygenated blood into the lungs, and the left side pumps oxygenated blood into the circulatory system. In this dissertation, as is common in the field, we focus on the left ventricle. This is partly for simplicity, but also because the left ventricle is under the highest pressure of the four sections by far [50], and thus the most prone to developing lethal arrhythmias [64].

Broadly, the cardiac cycle can be broken into the diastole, or filling phase, and the systole, or ejection phase [50]. The filling of the ventricles with blood occurs passively due to a pressure difference, with suction resulting from the release of elastic strain energy [49]. In contrast, the ejection of blood from the atria into the ventricles and from the ventricles into the circulatory system is an active process, which we attribute to the strain created by contraction of the muscle fibers [49].

This leads us to the microscopic level. Cardiac tissue is composed of excitable muscle cells, called cardiomyocytes, arranged in helical bundles running parallel to one another and separated by sheets of collagen. Cardiomyocytes are shaped like elongated cylinders, typically $80 - 100\,\mu$m long, with a radius of $5 - 20\,\mu$m [21]. The tissue forms three layers — the endocardium (inner tissue), myocardium (core tissue), and epicardium (outer tissue) — to make up the ventricular and atrial walls
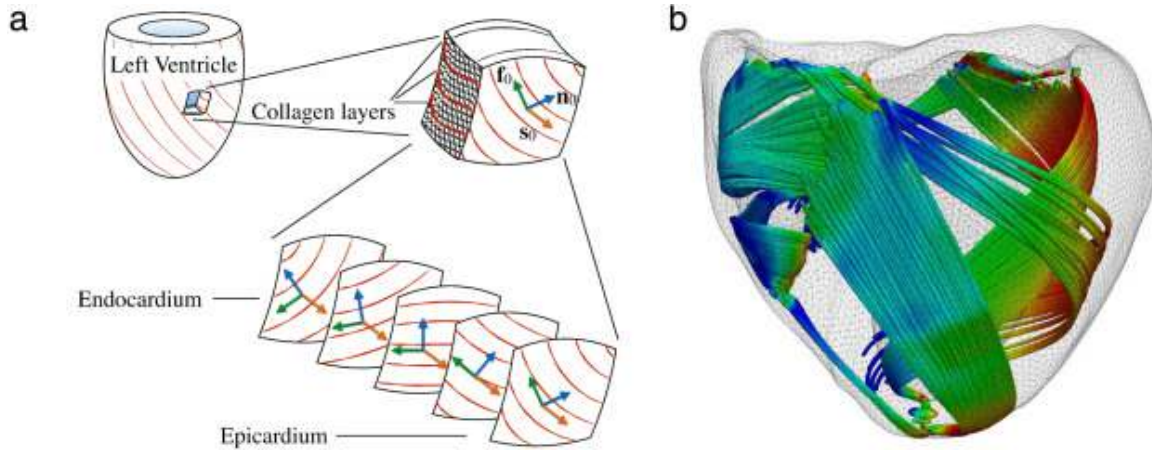
Figure 1.2: Simplified diagram of ventricular tissue layers (a) and transmural configuration of muscle fibers and laminar sheets (a-b). Figure taken from [52].

(see Figure 1.2). Though the boundaries between them are not known exactly, the layers do exhibit slightly different properties [41]; O'Hara et al. [47] present a dataset for the differences between cells in each layer to complement their highly detailed model of human action potential.

The heart's activation system is largely calcium-based. An *action potential*, or rapid rise and fall of transmembrane potential, develops automatically in so-called pacemaker cells in the sinoatrial node [50]. Gap junctions between cells allow for the transmission of the action potential through the tissue, its arrival triggering the movement of ions across the cell membrane. Inward currents (largely Na^+) are responsible for depolarizing, and thus exciting, cardiac cells, while outward currents (largely K^+) repolarize the membrane to its resting potential [36]. Depolarization opens calcium channels in the cell membrane, allowing a slower inward current of Ca^{2+} to form. This triggers a larger release of Ca^{2+} from the sarcoplasmic reticulum, known as *calcium-induced-calcium-release*. The subsequent rise in intracellular Ca^{2+} initiates a response in the muscle fibers, whereby thick filaments (known as myosin) bind to and pull on thin filaments (known as actin), resulting in contraction [54]. This electrically-induced mechanical response is often called *excitation-contraction coupling*, and is an important link between the mechanical and electrophysiological systems in the heart. A simplified version of this process is depicted in Figure 1.3.

The arrangement of the cardiac fibers is critical to both the electrical and mechanical aspects of cardiac function. The calcium-based activation signal travels up to four times faster along the fiber axis than in the sheet and normal directions [21, 41, 52]. Furthermore, the contraction caused by the interaction of actin and myosin occurs
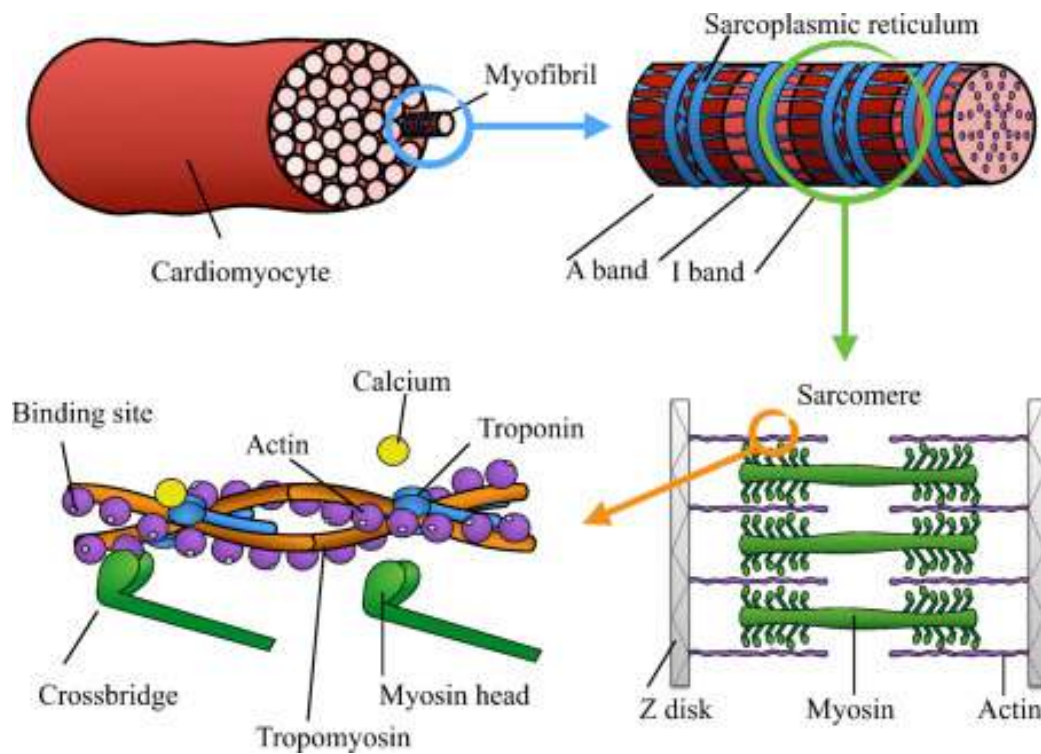
Figure 1.3: Simplified diagram of a cardiac cell, depicting its contractile mechanism. Figure taken from [52].

along the fiber direction, causing directionally heterogeneous active strain in the ventricular wall [6, 41, 49]. The orientation of the fibers also dictates the manner in which the heart can bend and twist, governing, for example, the shortening of the left ventricle from apex to base during contraction [6, 15, 58].

We have omitted a great deal of detail in this overview of the cardiac cycle and physiology. While we have barely scratched the surface in either respect, we hope that this chapter has succeeded in providing a glimpse into the complexity of the heart and motivating the manner in which we attempt to reconstruct it mathematically.

Chapter 2

Mathematical Models

2.1   General Approach

This project deals with the numerical approximation of the active contraction of the cardiac muscle, and the representation of mechanoelectrical feedback (MEF) using a recent model of stress-assisted diffusion (SAD) [16]. We thus require a model that describes both the mechanical and electrical properties of cardiac tissue. We describe the mechanics using theories from nonlinear elasticity and continuum mechanics, which are appropriate for describing the large deformations seen during the cardiac cycle and approximating the collective behavior of cardiomyocytes. We adopt an orthotropic *constitutive law* proposed by Holzapfel and Ogden [30], which expresses the experimentally observed relationship between stress and strain [45]. We couple this with a four-variable phenomenological model of human action potential, developed by Bueno-Orovio et al. [10].

In this chapter, we describe both the mechanical and electrophysiological components of our model. We then discuss the coupling between the two, including SAD and active tension generation. Finally, we describe the calculation of the fiber and sheetlet directions, which is the extra step required to extend the model to 3D.

2.2   Mechanical Model

We consider a deformable body in its reference configuration $\Omega \subset \mathbb{R}^d$, $d \in \{2, 3\}$, with piecewise smooth boundary $\partial\Omega$. We define $\mathbf{x_0}$ to be a point in Ω, such that $\boldsymbol{u}(\mathbf{x_0}, t) = \mathbf{x}(\mathbf{x_0}, t) - \mathbf{x_0} : \Omega \to \mathbb{R}^d$ denotes a displacement field describing the new position $\mathbf{x}$ in the deformed, or *current*, configuration Ω_t (see Figure 2.1). The motion from point to point is written as $\mathbf{x} = \mathcal{X}(\mathbf{x_0}, t)$. An important measure of deformation in nonlinear continuum mechanics is the deformation gradient $\mathbf{F} = \mathbf{I} + \nabla\boldsymbol{u}$, which
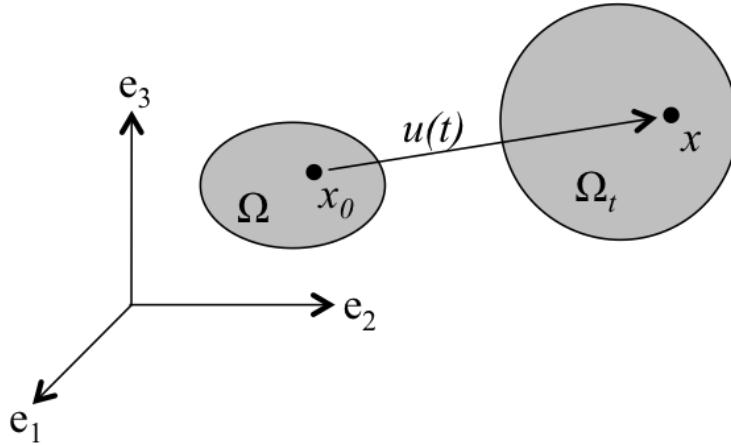
Figure 2.1: Displacement field of a particle.

maps tangent vectors in the reference configuration to tangent vectors in the current configuration [29]. Its Jacobian determinant, $J = \det \mathbf{F} = \rho_0/\rho$, gives the change in volume due to deformation, where ρ_0 and ρ indicate density of the undeformed and deformed material, respectively. With no motion, $\mathbf{F} = \mathbf{I}$, and with no change in volume, $J = 1$. Each of these measures of deformation is essential to our model because the nature of the tissue's movement is not known in advance [56].

We define two stretch tensors, $\mathbf{C} = \mathbf{F}^{\mathsf{T}}\mathbf{F}$ and $\mathbf{B} = \mathbf{F}\mathbf{F}^{\mathsf{T}}$, as the right and left Cauchy-Green deformation tensors, respectively. We base our measures of strain on $\mathbf{C}$, defining its first isotropic invariant as

$$\mathcal{I}_1(\mathbf{C}) = \mathrm{tr}(\mathbf{C}),$$

and its anisotropic, or directionally dependent, pseudo-invariants as

$$\mathcal{I}_{4,f} = \mathbf{f_0} \cdot \mathbf{Cf_0} = \mathbf{f} \cdot \mathbf{f}, \quad \mathcal{I}_{4,s} = \mathbf{s_0} \cdot \mathbf{Cs_0} = \mathbf{s} \cdot \mathbf{s}, \quad \mathcal{I}_{8,fs} = \mathbf{f_0} \cdot \mathbf{Cs_0} = \mathbf{f} \cdot \mathbf{s}.$$

$\mathcal{I}_{4,i}, i \in \{f, s\}$ measure direction-specific stretch, and $\mathcal{I}_{8,fs}$ concerns the angle spanned by $\mathbf{f}$ and $\mathbf{s}$ and the relative shear between these directions [26]. Our undeformed coordinate system is defined by $(\mathbf{f_0}(\mathbf{x}), \mathbf{s_0}(\mathbf{x}), \mathbf{n_0}(\mathbf{x}))$, corresponding to the local preferred directions of cardiac fibers, transversal collagen sheetlets, and the normal cross-fiber field $\mathbf{n_0} = \mathbf{f_0} \times \mathbf{s_0}$, respectively (Figure 2.2). This mutually orthogonal coordinate system is necessary to describe the myocardium tissue, which is an *orthotropic* material displaying distinct behavior in each direction [30]. While some studies opt instead for a simpler isotropic or transversely isotropic material law, the consensus in the field is that an orthotropic law is required to accurately represent cardiac tissue [52]. In 2D, we align $\mathbf{f_0}(\mathbf{x})$ and $\mathbf{s_0}(\mathbf{x})$ with the x- and y- axes, but in 3D, calculation of
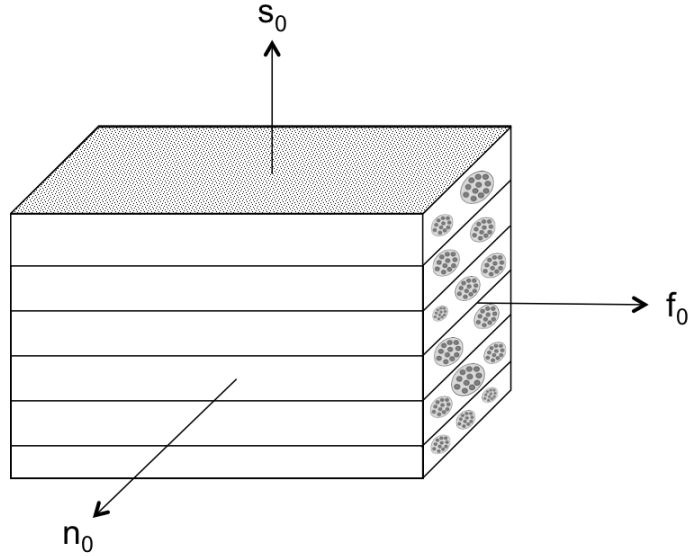
Figure 2.2: Simplified diagram of cardiac tissue, depicting its locally orthonormal coordinate system.

the fiber fields requires further computation to account for rotational anisotropy (see Section 2.5).

We adopt the constitutive model proposed in Holzapfel and Ogden [30]. Treating the cardiac tissue as a hyperelastic medium, we derive its first Piola-Kirchhoff stress tensor from a strain-energy function, which is written in terms of the invariants of $\mathbf{C}$ to guarantee frame indifference [6]. We write

$$\Psi_{\text{pas}}(\mathbf{F}) = \frac{a}{2b}\mathrm{e}^{b(I_1-d)} + \frac{a_{fs}}{2b_{fs}}\left[\mathrm{e}^{b_{fs}I_{8,fs}^2} - 1\right] + \sum_{i\in\{f,s\}}\frac{a_i}{2b_i}\left[\mathrm{e}^{b_i(I_{4,i}-1)_+^2} - 1\right], \qquad (1)$$

where a, b, a_i and b_i are material parameters, and $(\gamma)_+ := \gamma$ for $\gamma > 0$, and zero otherwise. The parameters used in our study are given in Table A.1, although it should be noted that these are generally determined through experimental observations, the results of which have been shown to vary depending on experimental setup [54].

2.2.1   Activation Mechanisms

We must also consider the ability of cardiac tissue to deform in the absence of external loads. This is typically done by adopting either an *active stress* or an *active strain* formulation. Rossi [53] carried out a qualitative comparison of the two formulations, and found that both are appropriate for modeling cardiac deformations. Details of anisotropic activations can be found in Usyk et al. [66] for active stress and Rossi et al. [55] for active strain descriptions.

While the active strain approach is adopted in many instances in the literature (for example, [6, 17, 49]), and is often favored due to the practicality of measuring strains directly using imaging techniques [53], the active stress approach is somewhat simpler and more natural for our needs. Our model incorporates stress-assisted diffusion, whereby the diffusion tensor depends explicitly on stress, as discussed in Section 2.4.1. Thus, solving for this quantity directly is convenient. We thus choose to adopt the active stress formulation for our 2D model, although we find that the active strain formulation better reproduces physiologically accurate deformation regimes in 3D; this will be further discussed in Section 2.5.

Active stress.   Following an active stress assumption, the activity of the muscle cells is accounted for by splitting the stress tensor into an active component and the standard passive component [3], such that

$$\mathbf{P} = \mathbf{P}_{\mathrm{pas}} + \mathbf{P}_{\mathrm{act}}. \tag{2}$$

It is typical to use $\mathbf{P}$, the *first Piola-Kirchhoff stress tensor*, when working in the reference configuration. A simple transformation gives us the Cauchy stress tensor $\boldsymbol{\sigma} = J^{-1}\mathbf{P}\mathbf{F}^{\intercal}$, which is natural to use when working in the current configuration.

We obtain our definition of $\mathbf{P}_{\mathrm{pas}}$ from Equation (1),

$$\mathbf{P}_{\mathrm{pas}} = \frac{\partial \Psi_{\mathrm{pas}}}{\partial \mathbf{F}} - pJ\mathbf{F}^{-\intercal}, \tag{3}$$

where p is solid hydrostatic pressure. We assume that the active stress component exhibits different behavior in each local direction, with its intensity depending on the degree of stretch in each direction and the scalar field of active tension T_a, whose dynamic behavior will be specified later on in Section 2.4.2. This gives us an orthotropic active stress tensor,

$$\mathbf{P}_{\mathrm{act}} = \frac{T_a}{I_{4,f}}\mathbf{F}\boldsymbol{f}_0 \otimes \boldsymbol{f}_0 + k\frac{T_a}{I_{4,s}}\mathbf{F}\boldsymbol{s}_0 \otimes \boldsymbol{s}_0 + k\frac{T_a}{I_{8,fs}}\mathbf{F}\boldsymbol{n}_0 \otimes \boldsymbol{n}_0. \tag{4}$$

Here, k is a positive constant representing transverse fiber stress development as a fraction of axial tension, set to $k = 0.3$ to agree with experimental results [66].

Check this is final version.

Active strain. An alternative approach is to instead decompose the deformation gradient into an active and passive component, such that

$$\mathbf{F} = \mathbf{F}_{\text{pas}}\mathbf{F}_{\text{act}}.$$

Equation (1) now defines $\Psi(\mathbf{F}_{\text{pas}})$, and Equation (3) now defines the entire first Piola Kirchoff stress tensor $\mathbf{P}$. Instead of defining an orthotropic model for $\mathbf{P}_{\text{act}}$, we adopt the orthotropic model for $\mathbf{F}_{\text{act}}$ used in Cherubini et al. [17],

$$\mathbf{F}_{\text{act}} = \mathbf{I} + \gamma_f \boldsymbol{f}_0 \otimes \boldsymbol{f}_0 + \gamma_s \boldsymbol{s}_0 \otimes \boldsymbol{s}_0 + \gamma_n \boldsymbol{n}_0 \otimes \boldsymbol{n}_0, \tag{5}$$

where the coefficients γ_i, $i \in \{f, s, n\}$ are smooth scalar functions of cell shortening ξ, describing the macroscopic stretch in each respective direction. These parameters serve as the analog to active tension T_a in the active stress formulation. Following the method proposed by Rossi et al. [55], we define these as

$$\gamma_f = \xi, \quad \gamma_s = (1 + \xi)^{-1}(1 + K_0\xi)^{-1} - 1, \quad \gamma_n = K_0\xi.$$

We use a simple sinusoidal function to represent ξ, and vary K_0 according to position within the wall.

2.2.2 Force Balance

We now consider force balance. By the balance of linear momentum, and adopting an incompressibility constraint, we have

$$\rho\,\partial_{tt}\boldsymbol{u} - \boldsymbol{\nabla} \cdot \mathbf{P} = \rho_0\boldsymbol{b} \qquad \text{in } \Omega \times (0, t_{\text{final}}], \tag{6a}$$

$$\rho J - \rho_0 = 0 \qquad \text{in } \Omega \times (0, t_{\text{final}}]. \tag{6b}$$

From here, we will assume zero body load such that $\boldsymbol{b} = \boldsymbol{0}$. We opt to retain the inertial term due to its potentially stabilizing effect, though its impact on the electrical and mechanical behavior of the tissue was found by Costabal et al. [20] to be minimal, and it is typical to assume quasistatic behavior [52].

The incompressibility constraint requires that volume is perfectly preserved, so that compression in one direction leads to extension in another. We require that tissue density is constant, and thus $J = 1$. This is a common and reasonable assumption, as studies cited in Holzapfel and Ogden [30] demonstrated, although cardiac tissue is not actually perfectly incompressible. The volume of the ventricular wall, which makes up a large portion of the total volume of the heart, actually changes significantly according to blood flow [26]. For this reason, some models adopt a

nearly-incompressible formulation, constructed using a penalty term (see, for example, [19, 26]).

Balance of angular momentum dictates that the Cauchy stress tensor $\boldsymbol{\sigma} = J^{-1}\mathbf{P}\mathbf{F}^{\mathsf{T}}$ must be symmetric, thus the Kirchhoff stress tensor $\boldsymbol{\Pi} = \mathbf{P}\mathbf{F}^{\mathsf{T}}$ is symmetric [29, 60]. Part of the novelty of our approach will be in dealing with $\boldsymbol{\Pi}$ rather than $\mathbf{P}$, motivated partly by the ease with which it can be stored computationally and the convenience of solving for a value explicitly used in our incorporation of SAD (discussed in Section 2.4).

2.2.3 Viscoelasticity

One potential modification of our model is to include viscoelastic effects. In a study by Sommer et al. [59], extension and shear tests demonstrated the viscoelastic (as well as nonlinear and orthotropic) properties of myocardial tissue, believed to be related to the molecule titin [44]. Indeed, all materials exhibit both elastic and viscous behavior – a purely elastic or purely viscous material is an idealization. Thus, although most cardiac models assume purely elastic behavior (including recent works [17] and [42]), this simple modification could make our model more realistic.

To incorporate viscosity, we can decompose the first Piola Kirchhoff stress tensor $\mathbf{P}$ into an elastic component and a viscous component,

$$\mathbf{P} = \mathbf{P}_{\mathrm{e}} + \mathbf{P}_{\mathrm{v}}. \tag{7}$$

Depending on whether one adopts the active stress or active strain formulation, $\mathbf{P}_{\mathrm{e}}$ may decompose into the active and passive components already discussed in Section 2.2.1.

Whereas elasticity concerns stress and strain, viscosity concerns the rate of strain [38]. We will thus construct the viscous component of stress by considering the rate of change of our deformation gradient and strain tensors. We derive these from $\mathbf{x}, \mathbf{u}$, and $\mathbf{F}$, using the methods described in Holzapfel [29]. Recalling that $\mathcal{X}(\mathbf{x_0}, t)$ is motion, we can write

$$\mathbf{F} = \frac{\partial \mathcal{X}(\mathbf{x_0}, t)}{\partial \mathbf{x_0}},$$
$$\dot{\mathbf{F}} = \frac{\partial}{\partial t}\left(\frac{\partial \mathcal{X}(\mathbf{x_0}, t)}{\partial \mathbf{x_0}}\right).$$

Note that this is equivalent to the *material* velocity gradient, referring to the reference configuration. We rewrite this as

$$\dot{\mathbf{F}} = \boldsymbol{\nabla}\mathbf{v}_0(\mathbf{x}_0, t),$$

and *push forward* into the current configuration to obtain the *spatial* velocity gradient,

$$\boldsymbol{\nabla}\mathbf{v}(\mathbf{x}, t) = \dot{\mathbf{F}}\mathbf{F}^{\mathsf{T}},$$

which will help us construct the rate of change of our Cauchy strain tensors. First, we decompose the spatial velocity gradient into the rate of deformation tensor and the spin tensor,

$$\mathbf{v}(\mathbf{x}, t) = \mathbf{d} + \mathbf{w} = \frac{1}{2}(\nabla\mathbf{v} + \nabla\mathbf{v}^{\mathsf{T}}) + \frac{1}{2}(\nabla\mathbf{v} - \nabla\mathbf{v}^{\mathsf{T}}).$$

We then have

$$\dot{\mathbf{C}} = 2\mathbf{F}\mathbf{d}\mathbf{F}^{\mathsf{T}}, \quad \dot{\mathbf{B}} = (\nabla\mathbf{v})\mathbf{B} + \mathbf{B}(\nabla\mathbf{v})^{\mathsf{T}}.$$

We adopt the model proposed by Karlsen [33], in which the viscous component of the Cauchy stress is given by

$$\boldsymbol{\sigma}_{\mathrm{v}} = \alpha e^{\beta \dot{I}_1}\dot{\mathbf{B}}. \tag{8}$$

Using a simple Piola transformation, we *pull back* to the reference domain and acquire the viscous component of the first Piola-Kirchhoff stress tensor,

$$\mathbf{P}_{\mathrm{v}} = J\boldsymbol{\sigma}_{\mathrm{v}}\,\mathbf{F}^{-\mathsf{T}}.$$

Throughout this dissertation, we perform simulations for both the hyperelastic and viscoelastic cases, offering a comparison of the two when possible. For further detail on the topic of viscoelasticity, we encourage the reader to consult Kumaran [38].

2.2.4   Full Mechanical System

We now define

$$\mathcal{G}(\boldsymbol{u}) := \frac{\partial \Psi_{\mathrm{pas}}}{\partial \mathbf{F}}\mathbf{F}^{\mathsf{T}} + \mathbf{P}_{\mathrm{act}}\mathbf{F}^{\mathsf{T}},$$

or, in the case of viscoelasticity,

$$\mathcal{G}(\boldsymbol{u}) := \frac{\partial \Psi_{\mathrm{pas}}}{\partial \mathbf{F}}\mathbf{F}^{\mathsf{T}} + \mathbf{P}_{\mathrm{act}}\mathbf{F}^{\mathsf{T}} + \mathbf{P}_{\mathrm{v}}\,\mathbf{F}^{\mathsf{T}}.$$

Then

$$\boldsymbol{\Pi} = \mathcal{G}(\boldsymbol{u}) - pJ\mathbf{I}, \tag{9}$$

motivating the interpretation of $\mathcal{G}(u)$ as the stress without a contribution from pressure. This definition is necessary in the active stress formulation, in which we wish to solve directly for Π.

We now have the components we require to model the mechanical behavior of cardiac tissue. Our full mechanical system consists of Equation (6a) written in terms of $\boldsymbol{\Pi}$, Equation (6b), and Equation (9):

$$\rho\,\partial_{tt}\boldsymbol{u} - \boldsymbol{\nabla}\cdot\boldsymbol{\Pi}\mathbf{F}^{-\mathsf{T}} = \mathbf{0}, \tag{10a}$$

$$J - 1 = 0, \tag{10b}$$

$$\boldsymbol{\Pi} - \mathcal{G}(\boldsymbol{u}) + pJ\mathbf{I} = \mathbf{0}, \tag{10c}$$

endowed with appropriate boundary conditions according to the particular experimental setting. In 2D, we assume a robin boundary condition,

$$\boldsymbol{\Pi}\mathbf{F}^{-\mathsf{T}}\boldsymbol{\nu} + \eta J\mathbf{F}^{-\mathsf{T}}\boldsymbol{u} = \mathbf{0} \quad \text{on } \partial\Omega \times (0, t_{\mathrm{final}}], \tag{11}$$

where $\boldsymbol{\nu}$ is the outward unit normal vector on $\partial\Omega$, and η is a stiffness coefficient. This type of boundary condition is a good choice as it allows enough movement to simulate the flexibility of real tissue, but satisfies the need to restrict the movement of the boundary to ensure well-posedness. In 3D, we used mixed boundary conditions to fix the ventricular base and simulate the pressure exerted by blood flow; the exact forms of these conditions are given in Section 2.5.

Recall that the goal of this dissertation is to advance the theoretical framework for modeling cardiac electromechanics. We have now outlined the mechanical component of our model, and we continue by describing the electrical component.

2.3 Electrophysiological Model

The other main component of our model is a four-variable *phenomenological* model for human action potential, developed by Bueno-Orovio et al. [10]. This model is simpler than more detailed *physiological* models ([31] and [63] for example, with up to 67 variables), but is considered to be the minimal model required to reproduce physiological action potential morphologies. In fact, the flexibility of the minimal model allows it to recreate the morphologies produced by the Ten Tusscher et al. [63] physiological model simply by tuning parameters. Because of the computational costs involved in our work, augmented by the technical complexity of coupling with the mechanical equations and eventually solving on a realistic 3D domain, the Bueno-Orovio et al. [10] model's minimal computational requirements are of great benefit.

This is also the motivation behind the choice to work with a *monodomain* model of electrical propagation as opposed to a *bidomain* model. In differentiating between the intracellular and extracellular domains, the bidomain model is more physiologically accurate because it accounts for the potential difference across the cell membrane [61]. Reduction to the monodomain model is a nontrivial simplification, requiring an assumption of equal anisotropy rates in the two domains. However, it is advantageous in its computational efficiency, and is thus common practice in the field [9, 53]. Multiple studies have investigated the differences in the results given by each model, and the consensus is that the difference is extremely small (1–2%), and smaller than the error introduced by discretization [9, 51]. Extension to the bidomain model is not of great difficulty, but at this time, we do not consider it to be a priority worth the extra computational cost.

Despite these simplifications, however, the Bueno-Orovio et al. [10] model adds additional accuracy and complexity beyond what is accounted for in similar existing studies. The modified two-variable Karma [34] model used in Cherubini et al. [17] and the three-variable Fenton and Karma [21] model used in Loppini et al. [42] are sufficient for capturing some important features, but fail to properly represent the morphology of the human action potential. Furthermore, it is important to note that the Bueno-Orovio et al. [10] model is specific to human ventricular action potentials, unlike the simpler models which were fitted to generic cells.

The propagation of electric potential v in cardiac tissue can be described by a reaction-diffusion system,

$$\chi \frac{\partial v}{\partial t} - \nabla \cdot (\mathbf{D} \nabla v) = I_{\text{ext}} - g(v, \vec{r}) \qquad \text{in } \Omega \times (0, t_{\text{final}}], \qquad (12\text{a})$$

$$\frac{d\vec{r}}{dt} = \vec{m}(v, \vec{r}) \qquad \text{in } \Omega \times (0, t_{\text{final}}], \qquad (12\text{b})$$

where χ is the ratio of membrane area to tissue volume, $\mathbf{D}$ is the conductivity tensor, $\vec{r}$ are ionic quantities, and I_{ext} is a spatio-temporal external stimulus applied to the medium (defined in Section 3.2). We impose a no-flux boundary condition and the initial conditions proposed in Bueno-Orovio et al. [10],

$$\mathbf{D} \nabla v \cdot \boldsymbol{\nu} = 0 \qquad \text{on } \partial\Omega \times (0, t_{\text{final}}], \qquad (13\text{a})$$

$$v = 0 \qquad \text{in } \Omega \times \{0\}, \qquad (13\text{b})$$

$$\vec{r} = [1, 1, 0] \qquad \text{in } \Omega \times \{0\}, \qquad (13\text{c})$$

where $\boldsymbol{\nu}$ is the outward unit normal vector on $\partial\Omega$. We emphasize that $\mathbf{D}$ is a tensor quantity to allow for directional differences in the conductivity properties of cardiac tissue [61]. We can rescale the dimensionless variable v to dimensions of mV within the physiological range using the relation $V_{mV} = 85.7v - 84$.

We assume that the total ionic current consists of a *fast inward* (fi), *slow inward* (si) and *slow outward* current (so),

$$g(v, \vec{r}) = g^{\text{fi}}(v, \vec{r}) + g^{\text{si}}(v, \vec{r}) + g^{\text{so}}(v, \vec{r}),$$

where the adimensional individual currents are given by

$$\chi \, g^{\text{fi}}(v, \vec{r}) = -r_1 \mathcal{H}(v - \theta_1)(v - \theta_1)(v_v - v)/\tau_{\text{fi}},$$

$$\chi \, g^{\text{si}}(v, \vec{r}) = -\mathcal{H}(v - \theta_2)r_2 r_3/\tau_{\text{si}},$$

$$\chi \, g^{\text{so}}(v, \vec{r}) = (v - v_0)(1 - \mathcal{H}(v - \theta_2))/\tau_o + \mathcal{H}(v - \theta_2)/\tau_{\text{so}}.$$

The kinetics of the *gating variables* $\vec{r}$ are given by

$$\vec{m}(v, \vec{r}) = \begin{pmatrix} (1 - \mathcal{H}(v - \theta_1))(r_{1,\infty} - r_1)/\tau_1^- - \mathcal{H}(v - \theta_1)r_1/\tau_1^+ \\ (1 - \mathcal{H}(v - \theta_2))(r_{2,\infty} - r_2)/\tau_2^- - \mathcal{H}(v - \theta_2)r_2/\tau_2^+ \\ ((1 + \tanh(k_3(v - v_3)))/2 - r_3)/\tau_3 \end{pmatrix}.$$

Here $\mathcal{H}$ is the Heaviside step function, and the time constants and infinite values are defined as:

$$\tau_1^- = (1 - \mathcal{H}(v - \theta_1^-))\tau_{1,1}^- + \mathcal{H}(v - \theta_1^-)\tau_{1,2}^-,$$

$$\tau_2^- = \tau_{2,1}^- + (\tau_{2,2}^- - \tau_{2,1}^-)(1 + \tanh(k_2^-(v - v_2^-)))/2$$
$$\tau_{\text{so}} = \tau_{so,1} + (\tau_{so,2} - \tau_{so,1})(1 + \tanh(k_{\text{so}}(v - v_{\text{so}})))/2$$
$$\tau_3 = ((1 - \mathcal{H}(v - \theta_2))\tau_{3,1} + H(v - \theta_2)\tau_{3,2},$$
$$\tau_o = ((1 - \mathcal{H}(v - \theta_0))\tau_{o,1} + H(v - \theta_0)\tau_{o,2}$$
$$r_{1,\infty} = \begin{cases} 1, & v < \theta_1^- \\ 0, & v \geq \theta_1^- \end{cases},$$
$$r_{2,\infty} = ((1 - \mathcal{H}(v - \theta_0))(1 - v/\tau_{2,\infty}) + \mathcal{H}(v - \theta_0)r_{2,\infty}^*.$$

The model proposed in Bueno-Orovio et al. [10] has a heterogeneous character that we do not consider in our study. They develop separate parameter sets to reproduce experimental results for the epicardium, myocardium and endocardium, as well as parameter sets that mimic the results of two more complicated ionic models for human ventricular cells. For simplicity, we use the parameter set developed for the epicardium, assuming that it is consistent throughout the cardiac wall. These parameter values are given in Table A.2.

This section outlined our model for the evolution of voltage and ionic species during the cardiac cycle. At this point, we have the components necessary to describe both mechanical deformation and the propagation of action potential in cardiac tissue; in the next section, we consider the interaction of these subprocesses.

2.4 Electromechanical Coupling

A major focus of our model is electromechanical coupling, which we incorporate bidirectionally. We account for the effect of tissue deformation on conductivity via stress-assisted diffusion, and consider excitation-contraction coupling in our model of active tension.

2.4.1 Stress-Assisted Diffusion

Mechanoelectrical feedback (MEF) is the mechanism by which the mechanical deformation of the cardiac tissue influences its electrophysiological properties. There are two main mechanisms of MEF: stretch-activated channels, and the recently proposed stress-assisted diffusion (SAD), which describes the effect of tissue deformation on the spreading of the action potential through the tissue. Most of the literature addressing MEF does not include SAD, but rather incorporates stretch-activated channels

by including a second reaction term $i_{\mathrm{SAC}}(v, \mathbf{F})$ in the equation for v (12a). This term induces an additional inward current that adds to the depolarization in the form

$$i_{\mathrm{SAC}}(v, \mathbf{F}) = C\left(\sqrt{I_{4,f}} - 1\right)(v - E),$$

where E and C are the reversal potential and the maximal conductance of the channels, respectively. This term is active only in the case of positive strains, or $I_{4,f} \geq 1$ (see [36]). In our study, we focus exclusively on SAD, but we refer the interested reader to Loppini et al. [42] for a comparison of the two mechanisms.

We include the phenomenon of SAD by constructing the conductivity tensor $\mathbf{D}$ such that it depends directly on the Kirchhoff stress. This is one reason why it is convenient to solve for stress directly in our model. We advance the theoretical framework put forward in previous works, incorporating the anisotropy introduced by stress proposed in Cherubini et al. [16] (and later exploited for simplified 2D cardiac electromechanics in Loppini et al. [42]), as well as the inherent anisotropy proposed in Cherubini et al. [17]. We set

$$\mathbf{D}(v, \mathbf{F}, \mathbf{\Pi}) = [D_0 + D_1 v]J\mathbf{C}^{-1} + D_0 J\mathbf{F}^{-1}\boldsymbol{f}_0 \otimes \boldsymbol{f}_0\mathbf{F}^{-\intercal}/2 + D_2\mathbf{F}^{-1}\mathbf{\Pi}\mathbf{F}^{-\intercal}, \qquad (14)$$

where the values for $D_i, i = \{0, 1, 2\}$ are displayed in Table A.3. We adopt the value of D_0 calculated in Bueno-Orovio et al. [10] specifically for human ventricular cells. The values of D_1 and D_2 are selected such that D_0 is the dominant coefficient.

The first term accounts for linear and nonlinear conductivity, or self diffusion depending on v. The second term accounts for anisotropy by encouraging diffusion in the direction of the fiber fields. The third term accounts for stress-assisted diffusion, whereby diffusion increases in areas of higher stress. The inclusion of both voltage- and stress-dependent terms in the conductivity tensor is, to our knowledge, a novel element of our model.

This definition of the conductivity tensor is an example of *strong coupling*, whereby the monodomain equations depend on the deformed configuration [19]. A Piola transformation is thus required to pull back into the reference configuration, which is why each term includes a factor of $\mathbf{C}^{-1} = \mathbf{F}^{-1}\mathbf{F}^{-\intercal}$. This nonlinear dependence of the conductivity tensor on the deformation gradient suggests strain-enhanced tissue conductivity (also referred to as geometric feedback [19]).

2.4.2 Active Tension

In the active stress formulation, the dependence of active mechanical deformation on excitation-contraction coupling is encoded through T_a, representing active tension in the cells. A simple model for active tension could be constructed using a sinusoidal function varying in time, for example, to mimic the tension generated during the cardiac cycle.

As discussed in Section 1.3, however, excitation-contraction coupling is largely calcium-driven. We thus develop a simplified model for active tension T_a depending only on calcium dynamics. The Bueno-Orovio et al. [10] model does not explicitly account for calcium, but its dynamics are approximately represented by the model's third gating variable r_3 [52]. Using r_3 as a proxy for calcium concentration, we write

$$T_a - \alpha_1 D_0 \Delta T_a = \alpha_2 \, r_3, \tag{15}$$

where α_1 and α_2 are parameters determining the steepness of the gradient and the range of T_a, respectively, given in Table A.3. The smooth gradient produced by Equation (15) is appropriate as it ensures that active tension generation reflects the intracellular calcium concentration, but not its fast dynamics. This also helps contribute to the regularization of stress and pressure, which will be discussed in Section 3.1.

It is also common to model active tension with a dependence on stretch, a nonlinear function of $\mathcal{I}_{4,f}$ [49, 52]. We opt to retain the formulation given in Equation (15) for now, although this could be an area for further development.

We have now discussed each of the main components of our electromechanical model of cardiac function: the mechanics, the electrophysiology, and the electromechanical coupling. We conclude this chapter by describing how we extend this coupled model to 3D.

2.5 Extension to 3D

Extension to 3D requires us to reconsider our boundary conditions, calculate fiber and sheetlet directions, and perhaps most importantly, consider the physiological accuracy of the model. Each of these components requires an understanding of the geometry in question. We thus begin with a description of our 3D domain; while this perhaps pertains more to the topic of Chapter 3, it is natural to discuss it here.
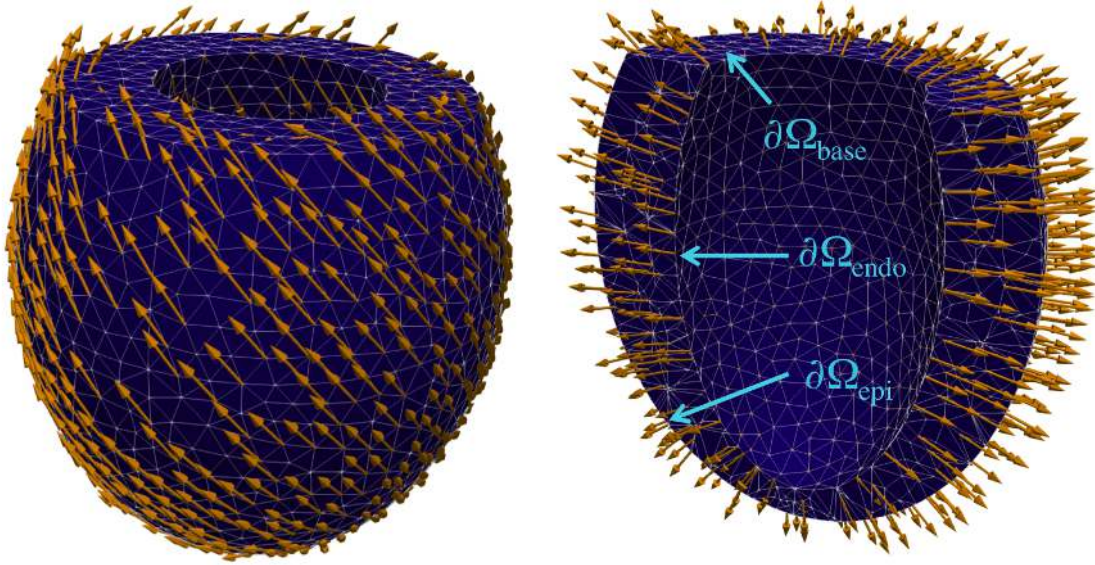
Figure 2.3: 3D domain for a simplified left ventricle, with fiber and sheetlet directions (left and right, respectively). The boundaries in Equations (17)-(19) and (20b) are denoted by $\partial\Omega_{\text{base}}$, $\partial\Omega_{\text{endo}}$, and $\partial\Omega_{\text{epi}}$.

3D Domain.   We implement our model on an idealized left-ventricular geometry. This consists of a truncated ellipsoid constructed with tetrahedral meshes using GMSH [25]. Our boundaries are defined by $\partial\Omega_{\text{base}}$, $\partial\Omega_{\text{endo}}$, and $\partial\Omega_{\text{epi}}$, which are clearly identified in Figure 2.3. We ultimately hope to implement our model on anatomically realistic meshes; implementing our model on this idealized geometry serves as a precursor to applying it to the more detailed geometries.

Boundary conditions.   We impose a zero normal displacement condition on the base, a traction condition consisting of a time-dependent pressure on the endo-cardium, and a Robin condition on the epicardium. The stiffness coefficient of the Robin condition varies spatially, following the method proposed in Cherubini et al. [17]. We define

$$\eta(y) := \frac{1}{y_b - y_a} \left[\eta_a(y_b - y) + \eta_b(y - y_a) \right], \tag{16}$$

where y_a and y_b denote the vertical positions of the apex and base, respectively, and η_a and η_b denote the stiffness coefficients of the apex and base, respectively. We require that $\eta_a < \eta_b$, so that stiffness is greatest at the base and decreases along the central axis. This reproduces the stiffness imposed by the contact of the muscle with

the aortic root, which is resistant to movement, and the more flexible pericardial sac and surrounding organs. Our boundary conditions are thus

$$\boldsymbol{u} \cdot \boldsymbol{\nu} = 0 \qquad\qquad \text{on} \quad \partial\Omega_{\text{Base}} \times (0, t_{\text{final}}], \qquad (17)$$

$$\mathbf{P}\boldsymbol{\nu} - p_N J \mathbf{F}^{-\mathsf{T}} \boldsymbol{\nu} = \mathbf{0} \qquad\qquad \text{on} \quad \partial\Omega_{\text{Endo}} \times (0, t_{\text{final}}], \qquad (18)$$

$$\mathbf{P}\boldsymbol{\nu} + \eta J \mathbf{F}^{-\mathsf{T}} \boldsymbol{u} = \mathbf{0} \qquad\qquad \text{on} \quad \partial\Omega_{\text{Epi}} \times (0, t_{\text{final}}], \qquad (19)$$

where $\boldsymbol{\nu}$ is the outward unit normal vector on $\partial\Omega$, p_N is a time-dependent prescribed boundary pressure, and η is the spatially-dependent stiffness given in Equation (16). We define a simple model for p_N,

$$p_N = p_0 \sin^2(\pi t),$$

to mimic the variation in the pressure exerted by the blood as it enters and leaves the ventricle. Values for η_a, η_b, and p_0 are given in Table A.1.

Calculation of fiber fields. To model cardiac activity in 3D we require the fiber and sheetlet directions, as both the mechanical and electrical systems are directionally heterogeneous (refer to Section 1.3). We can model these coordinates using the method of Rossi et al. [55], also used in Cherubini et al. [17], for example. We begin by defining the center axis of the left ventricle as a unit vector $\boldsymbol{k}_0$, pointing from apex to base. As we must account for rotational anisotropy within the ventricular wall, we set the limits of fiber rotation, or the endocardial and epicardial fiber angles, to $\theta_{\text{endo}} = 60°$ and $\theta_{\text{epi}} = -50°$, respectively.

We calculate sheetlet direction and position within the ventricular wall by solving a mixed Poisson problem for a potential ϕ and sheetlet direction ψ:

$$-\nabla \cdot \psi = 0 \quad \text{and} \quad \psi = \nabla\phi \quad \text{in } \Omega, \qquad (20\text{a})$$

$$\psi \cdot \boldsymbol{\nu} = 0 \text{ on } \partial\Omega_{\text{base}}, \quad \phi = 0 \text{ on } \partial\Omega_{\text{endo}}, \quad \phi = 1 \text{ on } \partial\Omega_{\text{epi}}. \qquad (20\text{b})$$

A discrete solution ψ_h is found using piecewise linear finite elements, and the final sheetlet directions are calculated by normalization, such that $\boldsymbol{s}_0 = \psi_h / \|\psi_h\|$. We then take the vector rejection of $\boldsymbol{k}_0$ from $\boldsymbol{s}_0$ (or the component of $\boldsymbol{k}_0$ orthogonal to $\boldsymbol{s}_0$), $\hat{\boldsymbol{k}}_0 = \boldsymbol{k}_0 - (\boldsymbol{k}_0 \cdot \boldsymbol{s}_0)\boldsymbol{s}_0$, and cross its normalization with $\boldsymbol{s}_0$ to obtain the so-called flat fiber field, $\hat{\boldsymbol{f}}_0 = \boldsymbol{s}_0 \times \hat{\boldsymbol{k}}_0 / \|\hat{\boldsymbol{k}}_0\|$. These fibers lie in the sheetlet planes, but we must now account for rotational anisotropy, where the degree of rotation of the fibers depends

on their position within the wall, given by the potential ϕ. The correctly oriented fibers are thus given by

$$\tilde{\boldsymbol{f}}_0 = \hat{\boldsymbol{f}}_0 \cos\theta(\phi_h) + \boldsymbol{s}_0 \times \hat{\boldsymbol{f}}_0 \sin\theta(\phi_h) + \boldsymbol{s}_0(\boldsymbol{s}_0 \cdot \hat{\boldsymbol{f}}_0)[1 - \cos\theta(\phi_h)],$$

where $\theta(\phi_h) := [(\theta_{\text{epi}} - \theta_{\text{endo}})\phi_h + \theta_{\text{endo}}]/180\pi$ is the function defining fiber angle variation. Finally, we normalize, to obtain $\boldsymbol{f}_0 = \tilde{\boldsymbol{f}}_0/\|\tilde{\boldsymbol{f}}_0\|$. Our third direction is given by $\boldsymbol{n}_0 = \boldsymbol{f}_0 \times \boldsymbol{s_0}$, providing a set of locally orthonormal coordinates. This can be seen in Figure 2.3, where the arrows indicate the fiber directions (left) and sheetlet normal directions (right). We note that this method works well only for single ventricle models; for biventricular geometries, the method must be redefined.

Physiological accuracy.   Preliminary inspection reveals that our mechanical system using the active stress formulation does not yield physiologically accurate deformations when implemented on the 3D domain. Due to the contraction of cardiac muscle fibers along their axis in response to electrical activation, we should see contraction of the ventricle in the upward direction against a rigid base. To satisfy incompressibility, this should be complimented by a thickening of the ventricular wall [15, 58]. However, our model of active stress displays stretching in the downward direction instead. To investigate this, we implement the active strain formulation in 3D and compare the two models.

(a)   (b)
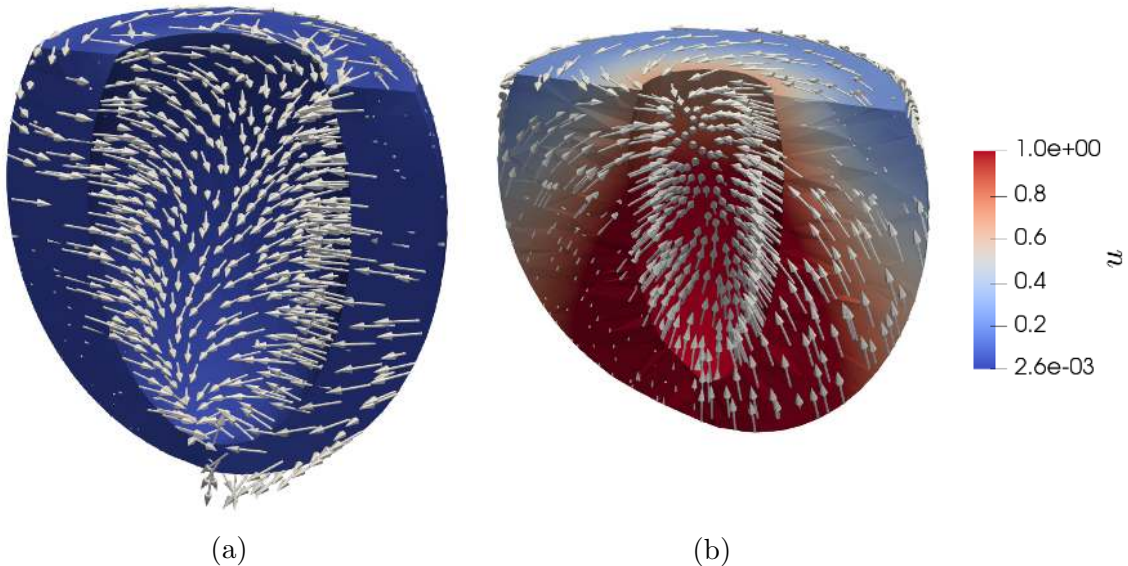
Figure 2.4: Comparison of displacement in active stress and active strain regimes. Ventricle color represents magnitude of displacement, while arrows indicate displacement direction.

Figure 2.4 shows a cross section of the ventricle at $t = 500\,\mathrm{ms}$ for both formulations, using the same parameter values where applicable. Note that both the stress and strain formulations result in torsion, or twisting, of the ventricle (which is expected), but only the active strain formulation yields wall-thickening and sufficient shortening from apex to base. These geometrical changes are important, as they facilitate the ejection of blood from the ventricle [15, 58]. For the sake of physiological accuracy, we thus conduct our 3D analysis of stress-assisted diffusion using the active strain formulation. While it lies outside the scope of this dissertation, the discrepancies between the models are of great importance, and will be the focus of future work.

Chapter 3

Numerical Methods

In this chapter, we describe the numerical algorithm used to implement our model. We also discuss the so-called S1-S2 stimulation protocol, which allows us to simulate the effect of reentrant arrhythmias. Finally, we present the idealized left ventricular geometry which we use to test our model in 3D.

3.1 Weak Formulation and Galerkin Discretization

To solve this system numerically, we use a mixed-primal finite element method (see [56] for details on a similar derivation). This method is widely recognized for being extremely versatile, particularly in its applicability to complicated geometries. The term *mixed* refers to the simultaneous approximation of different physical quantities, which is beneficial in that it respects the structure of our governing equations in the mechanical system. For the sake of simplicity, we concentrate the presentation in this section to the case of the active stress formulation; modification to the active strain formulation is straightforward. For a detailed explanation of the mixed finite element method, we refer to Gatica [23].

We consider the problem in its reference configuration, as the current configuration is unknown, and cast it into its variational form by integrating against test functions. For $t > 0$, find $(\boldsymbol{u}, p, \boldsymbol{\Pi}) \in \mathbf{H}^1(\Omega) \times \mathrm{L}^2(\Omega) \times \mathbb{L}^2(\Omega)$ and $(v, \vec{r}, T_a) \in [\mathrm{H}^1(\Omega)]^5$ such that

$$\int_\Omega \rho\, \partial_{tt} \boldsymbol{u} \cdot \boldsymbol{v} + \int_\Omega \boldsymbol{\Pi} : \nabla \boldsymbol{v}\, \mathbf{F}^{-\intercal} - \int_{\partial\Omega} \eta\, \mathbf{F}^{-\intercal}\, \boldsymbol{u} \cdot \boldsymbol{v} = \mathbf{0} \qquad \forall \boldsymbol{v} \in \mathbf{H}^1(\Omega), \quad (21\mathrm{a})$$

$$\int_\Omega [J - 1]\, q = 0 \qquad \forall q \in \mathrm{L}^2(\Omega), \quad (21\mathrm{b})$$

$$\int_\Omega [\boldsymbol{\Pi} - \mathcal{G}(\boldsymbol{u}) + pJ\mathbf{I}] : \boldsymbol{\tau} = 0 \qquad \forall \boldsymbol{\tau} \in \mathbb{L}^2(\Omega), \quad (21\mathrm{c})$$

$$\int_\Omega \frac{\partial v}{\partial t}\, w + \int_\Omega \mathbf{D}(v, \mathbf{F}, \boldsymbol{\Pi}) \nabla v \cdot \nabla w = \int_\Omega \left[g(v, \vec{r}) + I_{\mathrm{ext}} \right] w \qquad \forall w \in \mathrm{H}^1(\Omega), \quad (21\mathrm{d})$$

$$\int_\Omega \frac{\partial \vec{r}}{\partial t} \cdot \vec{s} = \int_\Omega \vec{m}(v, \vec{r}) \cdot \vec{s} \qquad \forall \vec{s} \in [\mathrm{H}^1(\Omega)]^3, \quad (21\mathrm{e})$$

$$\int_\Omega \alpha_1 D_0 \nabla T_a \cdot \nabla \varphi + \int_\Omega T_a\, \varphi = \int_\Omega \alpha_2\, r_3\, \varphi \qquad \forall \varphi \in \mathrm{H}^1(\Omega). \quad (21\mathrm{f})$$

Here we define $\mathrm{L}^2(\Omega)$ to be the Lebesgue space of square integrable functions on Ω, and $\mathrm{H}^1(\Omega)$ to be the Sobolev space of of square-integrable functions with square-integrable derivatives, that is

$$\mathrm{L}^2(\Omega) = \left\{ v : \int_\Omega v^2 dV < \infty \right\}, \quad \mathrm{H}^1(\Omega) = \left\{ v \in \mathrm{L}^2(\Omega) : \frac{\partial v}{\partial X_i} \in \mathrm{L}^2(\Omega),\, i = 1, ..., d \right\}.$$

We let $\mathbf{H}^1(\Omega) = \mathrm{H}^1(\Omega)^d$, and $\mathbb{L}^2(\Omega) = \mathrm{L}^2(\Omega)^{d \times d}$. Our choice of function space is motivated by the need to compute the gradients of v, w, T_a, and φ, and to satisfy regularity requirements.

It is important to note the significance of the three-field elasticity formulation. This approach allows us to avoid the phenomenon of *volumetric locking*, or unphysically small deformation, as discussed for the case of cardiac biomechanics in Baroli et al. [7]. While other methods exist to address this issue, such as using higher order elements [6], stabilized mixed formulations [57], or Lagrange multiplier-based methods [28], our approach not only prevents locking [39] but also directly solves for variables of interest [56]. This is particularly helpful in accommodating our model's electromechanical coupling, in which the the conductivity explicitly depends on the stress tensor.

The solvability analysis of nonlinearly coupled problems such as (21) is well beyond the scope of this dissertation. We mention nevertheless that the coupling of linear

elasticity and stress-assisted diffusion problems has been recently addressed in the context of mixed-primal formulations in Gatica et al. [24]. The tools required to establish well-posedness involve fixed-point theorems, compactness arguments, higher regularity, and the Babuška-Brezzi and Lax-Milgram theorem (for a simple review of these theorems, we again refer to Gatica [23]). For the case of hyperelasticity and nonlinear bidomain equations, the theoretical aspects involve much more technical arguments, and a first attempt has been advanced in Andreianov et al. [4]. The satisfaction of the requirements is still an area of active research in the community and so we simply proceed under the assumption that (21) is well-posed.

We discretize our problem using a mixed-primal Galerkin approach based on the variational form given above. We split Ω into triangles or tetrahedra K of maximum diameter h_K, and call this partition $\mathcal{T}_h$. The meshsize is then $h := \max\{h_K : K \in \mathcal{T}_h\}$. We seek a piecewise linear approximation of displacement, and piecewise constant approximations of solid pressure and Kirchhoff stress entries. All unknowns in the electrophysiological system (the voltage and gating variables) are approximated with Lagrange finite elements, which are piecewise linear and continuous. We seek our approximations in the finite-dimensional spaces $\mathbf{V}_h \subset \mathbf{H}^1(\Omega)$, $Q_h \subset \mathrm{L}^2(\Omega)$, $\mathbb{T}_h \subset \mathbb{L}^2(\Omega)$, $W_h \subset \mathrm{H}^1(\Omega)$, defined in the general case of arbitrary order $k \geq 0$, as follows:

$$\mathbf{V}_h := \{\boldsymbol{v}_h \in \mathbf{H}^1(\Omega) : \boldsymbol{v}_h|_K \in \mathbb{P}_{k+1}(K)^d, \forall K \in \mathcal{T}_h\},$$
$$Q_h := \{q_h \in \mathrm{L}^2(\Omega) : q_h|_K \in \mathbb{P}_k(K), \forall K \in \mathcal{T}_h\},$$
$$\mathbb{T}_h := \{\boldsymbol{\tau}_h \in \mathbb{L}^2(\Omega) : \boldsymbol{\tau}_h|_K \in \mathbb{P}_k(K)^{d \times d}, \forall K \in \mathcal{T}_h\},$$
$$W_h := \{w_h \in \mathrm{H}^1(\Omega) : w_h|_K \in \mathbb{P}_{k+1}(K), \forall K \in \mathcal{T}_h\},$$

where $\mathbb{P}_r(R)$ denotes the space of polynomial functions of degree $s \leq r$ defined on the set R. In the 2D case, we use lowest order elements ($k = 0$).

To discretize in time, we partition our time interval of interest $[t_0, t_{\max} = 600\,\mathrm{ms}]$ into discrete steps of size $\Delta t = t_{n+1} - t_n = 0.3\,\mathrm{ms}$. We select this temporal resolution based on the finding by Cherubini et al. [17] that this is the coarsest possible time step that produces conduction velocities in physiological ranges.

We use a first-order semi-implicit method to to solve for our unknowns at time t_{n+1}, letting x^{n+1} denote the value of a given variable x at time t_{n+1}. We use backward Euler time integration to advance the linear part of diffusion implicitly, but calculate nonlinear reaction terms and coupling via stress-assisted diffusion explicitly. The advantage of this scheme is that all nonlinear terms in the kinetic equations are

calculated from known quantities $(v_h^n, \vec{r}_h^n)$. Our fully discrete system can be expressed as follows:

For each $n = 0, 1, \ldots$: find $(\mathbf{\Pi}_h^{n+1}, \boldsymbol{u}_h^{n+1}, p_h^{n+1})$ and $(v_h^{n+1}, \vec{r}_h^{n+1}, T_{a,h}^{n+1})$ such that

$$\rho \int_\Omega \frac{u^{n+1} - 2u^n + u^{n-1}}{\Delta t^2} \cdot \boldsymbol{v}_h + \int_\Omega \mathbf{\Pi}_h^{n+1} : \nabla \boldsymbol{v}_h \mathbf{F}^{-\mathsf{T}}(\boldsymbol{u}_h^{n+1}) \tag{22a}$$

$$- \int_{\partial\Omega} \eta \mathbf{F}^{-\mathsf{T}}(\boldsymbol{u}_h^{n+1}) \boldsymbol{u}_h^{n+1} \cdot \boldsymbol{v}_h = 0 \quad \forall \boldsymbol{v}_h \in \mathbf{V}_h, \tag{22b}$$

$$\int_\Omega [J(\boldsymbol{u}_h^{n+1}) - 1] \, q_h = 0 \quad \forall q_h \in Q_h, \tag{22c}$$

$$\int_\Omega [\mathbf{\Pi}_h^{n+1} - \mathcal{G}(\boldsymbol{u}_h^{n+1}) + p_h^{n+1} J(\boldsymbol{u}_h^{n+1})] : \boldsymbol{\tau}_h = 0 \quad \forall \boldsymbol{\tau}_h \in \mathbb{T}_h, \tag{22d}$$

$$\int_\Omega \frac{v_h^{n+1} - v_h^n}{\Delta t} w_h + \int_\Omega \mathbf{D}(v_h^n, \mathbf{F}(\boldsymbol{u}_h^n), \mathbf{\Pi}_h^n) \, \nabla v_h^{n+1} \cdot \nabla w_h \tag{22e}$$

$$- \int_\Omega \left[g(v_h^n, \vec{r}_h^n) + I_{\text{ext}} \right] w_h = 0 \quad \forall w_h \in W_h, \tag{22f}$$

$$\int_\Omega \frac{\vec{r}_h^{n+1} - \vec{r}_h^n}{\Delta t} \cdot \vec{s}_h - \int_\Omega \vec{m}(v_h^n, \vec{r}_h^n) \cdot \vec{s}_h = 0 \quad \forall \vec{s}_h \in W_h, \tag{22g}$$

$$\int_\Omega \alpha_1 D_0 \nabla T_{a,h}^{n+1} \cdot \nabla \varphi_h + \int_\Omega T_{a,h}^{n+1} \varphi - \int_\Omega \alpha_2 r_3^n \varphi = 0 \quad \forall \varphi_h \in W_h. \tag{22h}$$

We find that with lowest order elements in the 2D case, our numerical method converges to a solution only in certain cases if the meshes are constructed from triangular and not quadrilateral cells. To address this, we stabilize the pressure by adding a bilinear jump term in the weak formulation of the problem. This effectively penalizes a jump in pressure between adjacent cells, minimizing the appearance of spurious oscillations in the solution. This type of modification can be found in the literature as a method of solving problems such as the Stokes' equations with low order finite elements [12, 46].

We reformulate the discrete incompressibility condition as

$$\int_\Omega [J - 1] \, q_h + \sum_{e \in \mathcal{E}_h} \int_e \kappa \, h_e [p_h]_h [q_h]_h = 0 \qquad \forall q_h \in Q_h, \tag{23}$$

where $e \in \mathcal{E}_h$ is an edge in the set of edges contained in the mesh, h_e is the length of a given edge, $[\gamma]_h$ indicates the jump in γ across the cell boundaries, and κ is a regularization parameter. After spatio-temporal discretization, this becomes

$$\int_\Omega [J(\boldsymbol{u}_h^{n+1}) - 1] \, q_h + \sum_{e \in \mathcal{E}_h} \int_e \kappa \, h_e [p_h^{n+1}]_h [q_h]_h = 0 \qquad \forall q_h \in Q_h. \tag{24}$$

We tune κ so that the adjustment to our original formulation is as small as possible so as not to disturb the structure of the problem, but large enough to penalize pressure jumps and provide stability. Note that only the discrete problem is actually affected, as there is no jump in the continuous case; thus, we have not modified our governing equations.

Of course, we must acknowledge that the scheme presented in (22) introduces lag into our system because we calculate the reaction terms with old data. With a small enough time step, however, this does not seem to cause a problem — the dynamics still behave as expected. Other more detailed reaction models require much more sophisticated time-advancing schemes, such as Rush-Larsen or many-stage Runge Kutta methods, for example. In our case, we accept the additional error in exchange for the computational benefits. Nevertheless, this is an area that future iterations of this model may well improve upon.

Considering the timescales on which these processes occur can further assist in reducing the computational load. Electrophysiological changes take place on a much faster timescale and with steeper spatial gradients than do mechanical changes, at least macroscopically. Thus, we solve the electrophysiological equations at each time step, but solve the mechanical equations at every 5th time step, such that $\Delta t_{\text{mech}} = 5 \cdot \Delta t_{\text{electro}}$. Some have further exploited these differences in discretization requirements, using a coarser spatial mesh for the mechanics than for the electrophysiology. However, with strong coupling between the mechanics and the electrophysiology, as we have, the imperfect overlap between different meshes would be problematic and increase model complexity [5].

We implement our model in FEniCS [2], an open-source computing platform for solving partial differential equations using the finite element method. By default, FEniCS solves nonlinear problems using Newton's method. We specify that the linear system occurring in the Newton iteration will be solved by LU factorization, with iterates terminating after a tolerance of $1e{-}7$ on the l^{∞}-norm of the residual has been achieved. We take advantage of the University of Oxford's remote machine *shadowcat*, with 36 cores and 768GB RAM, to run our code.

3.2 S1-S2 Excitation Protocol

The initiation, maintenance, prevention and treatment of so-called *reentrant waves* is a major focus of current research due to their implication in atrial and ventricular fibrillation [61]. We are thus interested in investigating the formation of spiral reentrant waves in our model setup, following the stimulation protocol described in Karma [35]. In 2D, we excite the entire left edge of the tissue with a stimulus labeled S1, creating a planar wave moving evenly through the tissue. An asymmetric stimulus (such as a square or strip), labeled S2, is then applied during the *vulnerable window* near the end of the refractory period, when some of the tissue has recovered excitability but depolarization is still blocked elsewhere. This causes unbalanced excitation, which can lead to the formation of a spiral wave. We will define the *spiral front* as the edge of the spiral wave, where the excitation front meets the repolarization waveback of the action potential. In our simulations, both waves have amplitude 3 and duration 3 ms. The S2 stimulus, occurring at $t = 330$ ms and $t = 335$ ms in 2D and 3D, respectively, is a square wave in the bottom left quadrant or octant, respectively. These stimuli are included as I_{ext} in Equation (12a). For example, in 2D, we have

$$I_{\text{ext}} = \begin{cases} 1, & x \leq 0.5\text{L}, \ y \leq 0.5\text{L}, \ t \in [335, 338], \\ 0, & \text{otherwise}, \end{cases} \tag{25}$$

where L is the side length of a square slab of tissue.

Chapter 4

Results and Analysis

In this chapter we present the results obtained from implementing our model in FEniCS [2]. In the interest of reproducibility, we have included basic examples of the code written for this dissertation in a GitHub repository located at
`https://github.com/ampropp/MMSC-Dissertation`.

4.1 Illustrating the Need for Pressure Stabilization

The pressure profile from simulations performed without and with the pressure stabilization modification are shown in Figure 4.1. These were conducted with $\alpha_2 = 0.01$ and $\eta = 0.001$. The difference is striking – the pressure stabilization method was extremely successful. The reader may thus assume that all 2D results that follow in this chapter were obtained using this pressure stabilization method.
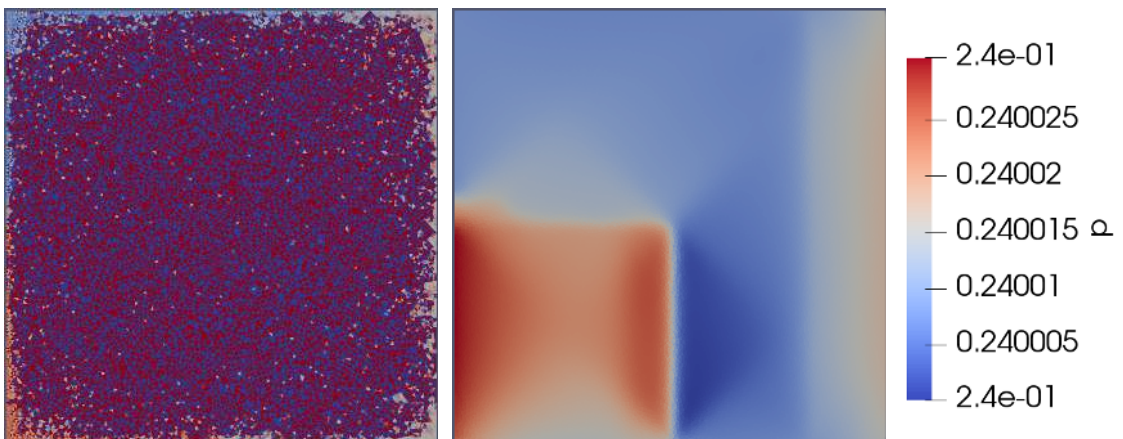

Figure 4.1: Comparison of pressure at $t = 348\,\text{ms}$ for simulations performed without (left) and with (right) the pressure stabilization modification. Simulations were performed under identical conditions except for the modification described in Section 3.

4.2   Verification of numerics

In order to verify our numerical method and investigate convergence, we construct an accuracy test using the method of manufactured solutions, following the method of Bürger et al. [11]. We conduct this analysis for the active stress formulation, with the constitutive law proposed by Holzapfel and Ogden [30] and given in Equation (1).

Considering a square 2D domain $\Omega = (0,1)^2$, we construct a smooth exact displacement, smooth exact transmembrane potential, and smooth reaction functions. We then calculate load and source terms that satisfy the governing equations. Finally, we measure errors between the exact and approximate solutions on meshes of increasing refinement, and evaluate the rate of convergence in suitable norms. We expect first order convergence due to our choice of finite element spaces.

We define a simplified steady-state system,

$$\Pi - \mathcal{G}(u) - pJ\mathbf{I} = 0,$$

$$-\nabla \cdot (\Pi \, \mathbf{F}^{-\intercal}) = f$$

$$T_a - \nabla \cdot (D_0 \, \nabla T_a) - w = g,$$

$$-\nabla \cdot ([D_0 J C^{-1} + D_1 J \mathbf{F}^{-1} \Pi \mathbf{F}^{-\intercal}] \, \nabla v) +$$

$$v + (1-v)\,vw = j,$$

$$w - w^2 + v = k,$$

which includes the monodomain equations, with stress-assisted diffusion and simple cubic and quadratic kinetics. Here, f, g, j and k are source terms constructed such that the closed-form solutions to the system defined above are given by the smooth functions

$$\Pi = \mathcal{G}(u) - pJ\mathbf{I}, \text{ constructed from } u, p, v, w, T_a,$$

$$u = \big(0.1\sin(\pi x)\,\cos(\pi y),\, 0.1\,\cos(\pi x)\,\cos(\pi y)\big),$$

$$p = 0.1\,\sin(\pi x)\,\sin(\pi y),$$

$$v = 0.1\,\cos(\pi x)\,\cos(\pi y),$$

$$w = 1 + 0.1\,\cos(\pi x)\,\sin(\pi y)\sin(\pi x),$$

$$T_a = 1 + 0.1\cos(\pi x)\sin(\pi y).$$

The results of this accuracy test are given in Tables 4.1 and 4.2. Error is calculated for each entity in its natural norm, and convergence rates are calculated as

$r(x) = \log\big(e(x)/\tilde{e}(x)\big) / \log(h/\tilde{h})$, where e and $\tilde{e}$ denote the errors generated on consecutive meshes of size h and $\tilde{h}$, respectively. We generally achieve the expected first-order convergence, and see that error is dominated by the approximation of Π and p.

Convergence of Mechanical Entities							
DoF	h	$e(\Pi)$	$r(\Pi)$	$e(u)$	$r(u)$	$e(p)$	$r(p)$
77	0.7071	43.2520	$--$	$3.761\,\mathrm{e}-02$	$--$	$3.016\,\mathrm{e}+01$	$--$
253	0.3536	27.1374	0.6725	$3.426\,\mathrm{e}-02$	0.3345	$1.903\,\mathrm{e}+01$	0.6647
917	0.1768	12.5351	1.1140	$2.166\,\mathrm{e}-02$	0.7615	$9.211\,\mathrm{e}+00$	1.0470
3493	0.0884	6.26365	1.0010	$1.181\,\mathrm{e}-02$	0.8751	$4.801\,\mathrm{e}+00$	0.9401

Table 4.1: Errors and convergence rates of approximate solutions Π_h, u_h, and p_h. Here, DoF denotes degrees of freedom, and h denotes the maximum cell size.

Convergence of Electrophysiological Entities							
DoF	h	$e(v)$	$r(v)$	$e(w)$	$r(w)$	$e(T_a)$	$r(T_a)$
77	0.7071	$1.528\,\mathrm{e}-01$	$--$	$1.926\,\mathrm{e}-01$	$--$	$1.562\,\mathrm{e}-01$	$--$
253	0.3536	$9.020\,\mathrm{e}-02$	0.7601	$1.069\,\mathrm{e}-01$	0.8499	$8.475\,\mathrm{e}-02$	0.8820
917	0.1768	$4.912\,\mathrm{e}-02$	0.8769	$5.739\,\mathrm{e}-02$	0.8968	$4.335\,\mathrm{e}-02$	0.9673
3493	0.0884	$2.818\,\mathrm{e}-02$	0.8016	$3.176\,\mathrm{e}-02$	0.8536	$2.183\,\mathrm{e}-02$	0.9896

Table 4.2: Errors and convergence rates of approximate solutions v_h, w_h, and $T_{a,h}$. Here, DoF denotes degrees of freedom, and h denotes the maximum cell size.

4.3   Conditions on Parameter D_2

Through a combination of linear stability analysis and inspection, we are able to loosely establish the range of values of D_2 for which we can obtain a solution. For this analysis, we assume fixed values of $D_0 = 1.171 \times 10^{-3}$ (proposed by Bueno-Orovio et al. [10]) and $D_1 = 9.0 \times 10^{-4}$. The difference of an order of magnitude ensures positive definiteness even at resting potential.

We determine that the condition required to retain parabolicity is

$$\frac{3}{2}D_0 + D_1 v + D_2 \mathbf{P}\left(1 + \frac{\partial u}{\partial x_0}\right) > 0,$$

as this ensures positive definiteness of $\mathbf{D}$, also required to satisfy the maximum principle [43]. We cannot determine exact conditions on D_2 because $\mathbf{D}$ depends on unknown

quantities whose ranges depend heavily on experimental setup. However, if D_2 is sufficiently small, it should be the case that $\mathbf{D}$ remains positive definite in most feasible situations.

Computational experiments reveal a window of values of D_2 for which our method converges. In the 2D hyperelastic case, we found that the upper bound for D_2 is approximately $D_2 = 7.5\,\mathrm{e}-3$, with the numerical solver failing to converge for larger values. In these simulations, stress achieved an L_2-norm of between 0.006 and 0.6. The viscoelastic case was able to accept larger values of D_2, up to $D_2 = 9.5\,\mathrm{e}-3$, with the L_2-norm of stress falling between 0.001 and 0.5. The 3D hyperelastic case achieved much higher levels of stress (with an L_2-norm of between 2 and 1200), and thus could only accept values of D_2 up to $D_2 = 3.5\,\mathrm{e}-5$. We did not find a difference in this respect between the hyperelastic and viscoelastic cases.

4.4   2D Results

In this section, we review the results produced by testing our model on a 2D slab of tissue with dimensions $12.0\,\mathrm{cm} \times 12.0\,\mathrm{cm}$. As we are mainly interested in the behavior of the tissue in response to a spiral wave, we consider the time interval $t \in [320\,\mathrm{ms}, 600\,\mathrm{ms}]$, with the S2 square wave stimulus occurring at $t = 330\,\mathrm{ms}$.

The formation and evolution of the spiral wave on its deforming domain (enlarged to $24.0\,\mathrm{cm} \times 24.0\,\mathrm{cm}$ for the purposes of visualization) can be seen in Figure 4.2. The spiral is initiated by the diffusion of voltage and ionic entities from the S2 stimulus into the leftmost section of the tissue, which has recovered enough excitability after S1. The wave then spreads outwards in all directions, engulfing the entire tissue except for the region that was just excited by the S2 wave. This spreading into the excitable regions forms a spiral-like shape that is self-stimulating.

4.4.1   Parameter Testing

We conducted a simple sensitivity analysis on our model's parameters for both the hyperelastic and viscoelastic cases. We conducted our analysis by increasing or decreasing either α_1, α_2 or η by one order of magnitude, holding the others constant at their reference values ($\alpha_1 = 10.0$, $\alpha_2 = 0.5$, and $\eta = 0.001$, as listed in Appendix A). This simple analysis therefore does not test for compounding or competitive effects.

We began by evaluating α_1 and α_2, the parameters governing active tension in Equation (15). Parameter α_1 helps determine T_a's smoothness, while α_2 controls its range. Our tests confirmed these effects, which are visible in Figure 4.3. We found

(a) $t = 350\,\mathrm{ms}$ (b) $t = 400\,\mathrm{ms}$ (c) $t = 450\,\mathrm{ms}$

(d) $t = 500\,\mathrm{ms}$ (e) $t = 600\,\mathrm{ms}$ (f) $t = 680\,\mathrm{ms}$

(g) $t = 800\,\mathrm{ms}$ (h) $t = 900\,\mathrm{ms}$ (i) $t = 1000\,\mathrm{ms}$
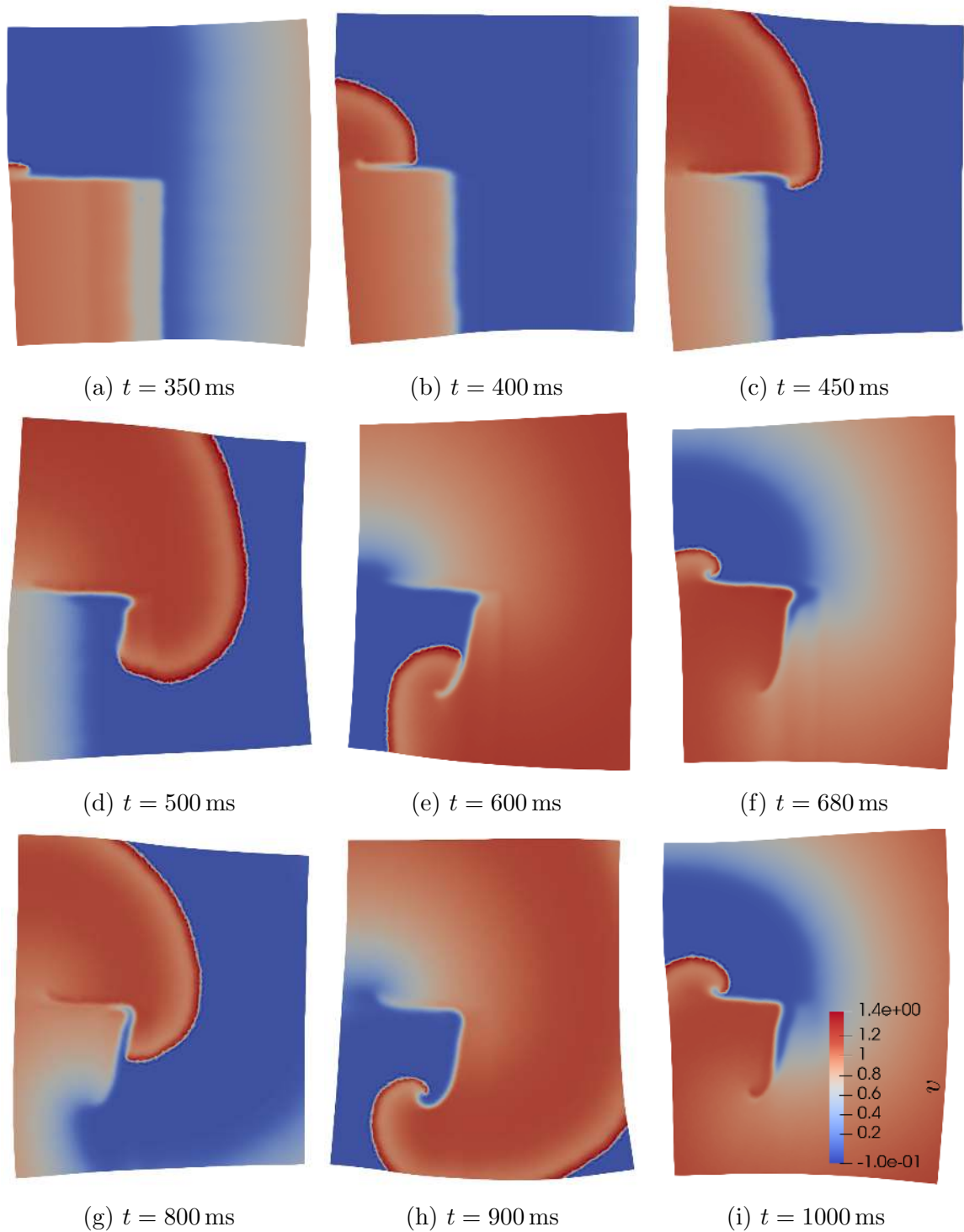
Figure 4.2: Evolution of voltage after S2 stimulus, showing formation of reentrant spiral wave on deforming tissue.

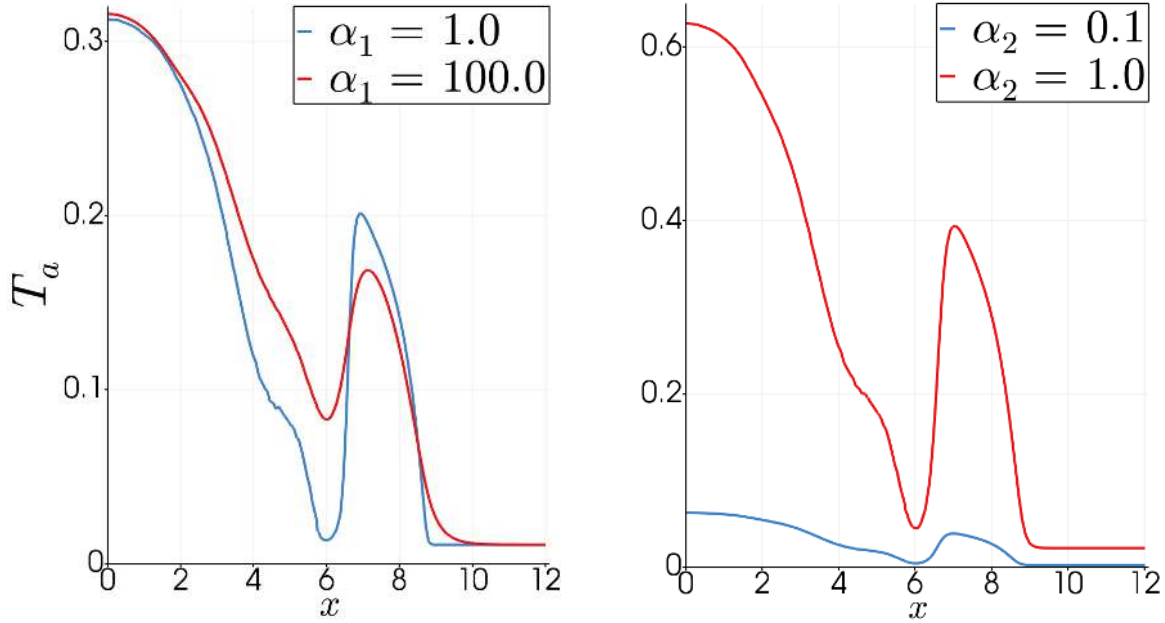Figure 4.3: Profiles of T_a taken across the tissue at $y = 6\,\mathrm{cm}$ and $t = 432\,\mathrm{ms}$ to evaluate the effect of parameters α_1 and α_2.

that larger values of α_1 produced smoother gradients in pressure and stress, while larger values of α_2 produced higher magnitude displacement, Kirchhoff stress, and pressure, as well as some more subtle changes in ionic quantities.

Parameter η determines the stiffness of the tissue. Decreasing η resulted an increase in the magnitude of displacement, stress, and pressure, as expected. However, the effect was extremely minimal, even across the three orders of magnitude tested ($\eta = 0.0001$ to $\eta = 0.01$). The effects on ionic entities were even smaller. This was the case for both the hyperelastic and viscoelastic cases.

Though these tests were not exhaustive, the fact that they yielded the expected results provides additional confidence in our model. Furthermore, our model's relatively low sensitivity to changes in the parameters implies that our choice of $\{\alpha_1, \alpha_2, \eta\}$ is likely not driving the dynamics we see in our more fundamental results (regarding viscoelasticity and SAD). The reader may assume from this point that $\alpha_1 = 10.0$, $\alpha_2 = 0.5$, and $\eta = 0.001$ in all 2D simulations (these values are also given in Table A.1 and Table A.3).

4.4.2 Effects of Viscosity

We found that accounting for viscous behavior in the tissue led to decreased displacement, stress, and pressure. This result was robust to every parameter combination

that we tested (see Section 4.4.1), and consistent spatially. The overall profiles of displacement, Kirchhoff stress, and pressure were similar between the viscoelastic and hyperelastic models, but more extreme in the hyperelastic case. This can be seen in Figure 4.4, which shows the profiles of the mechanical entities over a line segment crossing the tissue horizontally, and in Figure 4.5a, which shows an overlaid image of the deformed tissues for both cases.

We also saw subtle differences in the ionic quantities between the hyperelastic and viscoelastic cases, as shown in Figures 4.5b and 4.5c. The edge of the voltage gradient differed between the two, with slightly higher values in the hyperelastic case. The calcium concentration throughout the spiral wave was also slightly higher for the hyperelastic case. It is unsurprising that the changes in ionic quantities between the hyperelastic and viscoelastic cases were more subtle than the mechanical changes; viscoelasticity is accounted for in the mechanical equations, and thus affects ionic quantities only indirectly as a consequence of electromechanical coupling.

We proceeded to investigate the effects of changing the viscosity parameters. The parameter β from Equation (8) exerted very minimal influence over the observed dy-
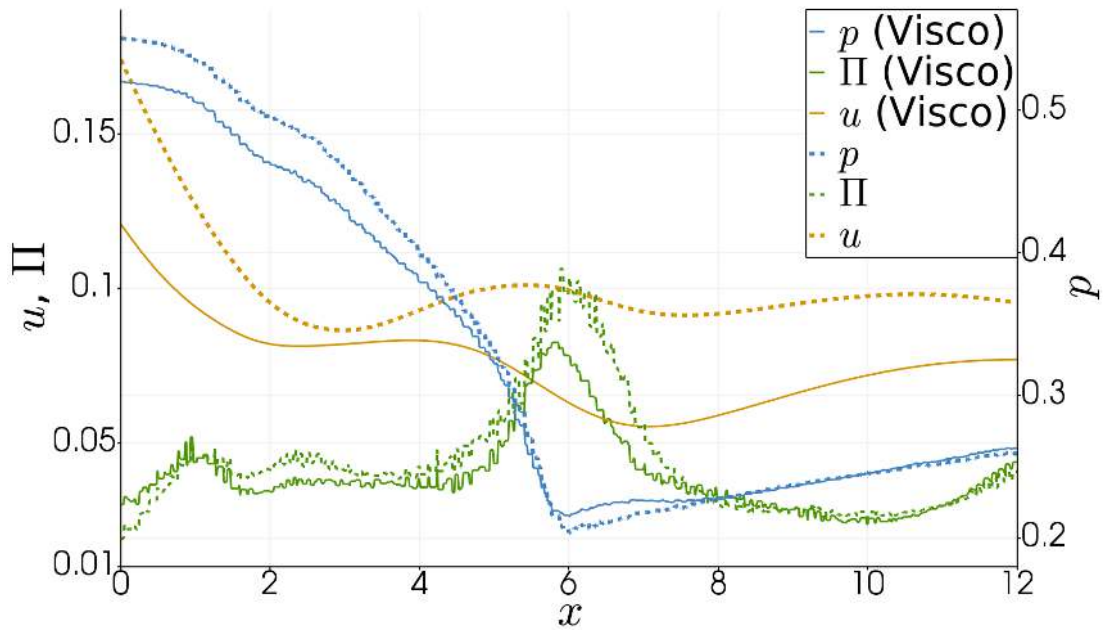

Figure 4.4: Comparison of mechanical entities between hyperelastic and viscoelastic models. The plots show the profiles of pressure, magnitude of stress, and magnitude of displacement over a line crossing the tissue horizontally at $y = 7\,\mathrm{cm}$, above the S2 stimulus region, at $t = 400\,\mathrm{ms}$. The dotted lines correspond to the hyperelastic model, and the solid lines to the viscoelastic model. Displacement, stress, and pressure are generally greater in the hyperelastic case.
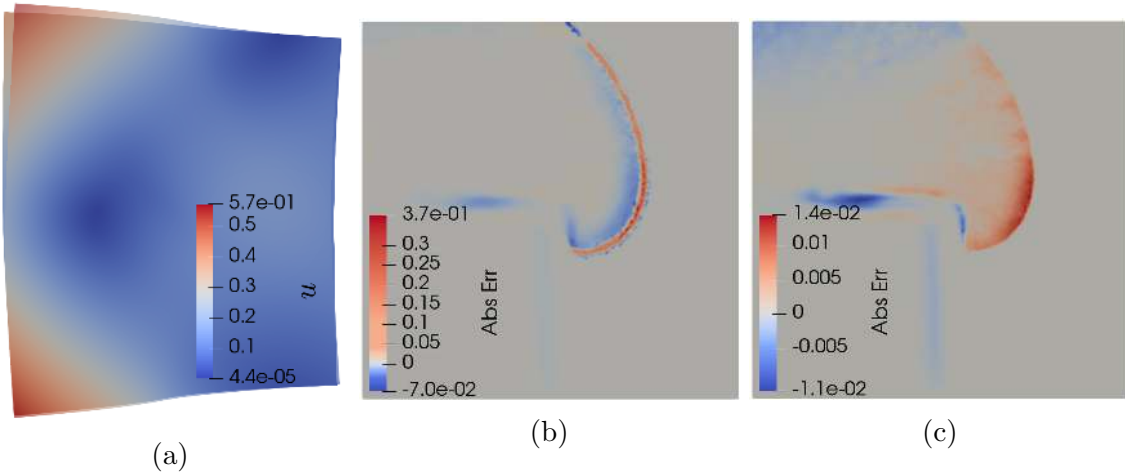
Figure 4.5: Comparison of hyperelastic and viscoelastic models at $t = 432\,\text{ms}$ on a zoomed-in section of tissue. (a) Displacement u on 2D domain, warped by magnitude of u. The more deformed hyperelastic tissue is reduced to 65% opacity to emphasize differences. (b) $v_{\text{hyper}} - v_{\text{visco}}$. (c) $r_{3,\text{hyper}} - r_{3,\text{visco}}$.

namics. Even for the five orders of magnitude tested, from $\beta = 0.0001$ to $\beta = 1.0$, the differences in displacement, voltage, and all other variables were minuscule. This could be because of the low rates of change of deformation that we see in our simulations.

We also tested values of γ across three orders of magnitude, from $\gamma = 2.26$ to $\gamma = 226.0$. As expected, increasing the value of γ, thereby increasing the viscoelastic contribution to Kirchhoff stress, magnified the differences between the hyperelastic and viscoelastic cases (essentially magnifying the effects seen in Figure 4.4). We also found that higher values of γ not only reduced the magnitude of Π, u, and p, but smoothed their profiles, reducing the distances between peaks and troughs.

Unless otherwise noted, the reader may assume from this point that $\beta = 0.01$ and $\gamma = 22.6$ in all 2D viscoelastic simulations. These values, proposed by Karlsen [33], ensure that the viscoelastic component is large enough to have an effect, but does not completely overwhelm the dynamics of the tissue.

4.4.3   Stress-Assisted Diffusion

In addition to determining the approximate range of D_2 for which we can find an approximate solution (Section 4.3), we also investigated the effect of D_2 on the tissue's response to the spiral wave. Figure 4.6 shows the differences in the ionic quantities between simulations with $D_2 = 1.0\,\text{e}-5$ and $D_2 = 5.0\,\text{e}-1$ at time $t = 388\,\text{ms}$, after the spiral has formed.

Closer inspection reveals that these differences were due to a difference in conduction velocity induced by SAD. In Figure 4.7, we see that conduction velocity was higher for larger values of D_2, or a larger SAD contribution. When the wave first emerged, the peak action potential was more advanced for the small D_2 case, but the large D_2 peak eventually caught up to and surpassed it. The ionic quantities followed the same trend. Indeed, an analysis similar to that which produced Figure 4.7 revealed that the overall profiles of the ionic quantities were highly similar between the two cases compared in Figure 4.6, but differed in the speed at which they moved through the tissue.

This effect on conduction velocity was not spatially consistent. SAD increased conduction velocity in the fiber (horizontal) direction, but actually decreased conduction velocity in the vertical and diagonal directions. This resulted in a noteworthy effect on the growth of the spiral wave. Figure 4.8 shows a comparison of the spiral wave in the viscoelastic case for two different values of D_2. The upper right area of the spiral is visibly flattened in the simulation with a larger value of D_2, suggesting that propagation of the voltage was suppressed in that direction. A similar effect was seen in the hyperelastic case.

Figure 4.9 provides another view of this effect. The voltage on the spiral front was initially higher for low D_2, meaning that the spiral wave emerged faster with a smaller SAD contribution. As the spiral grew, however, voltage on the horizontally-moving front became higher for large D_2. Thus, a larger SAD contribution caused the voltage to move faster in the fiber direction. In the upward, diagonal, and downward directions, however, we did not see this effect.

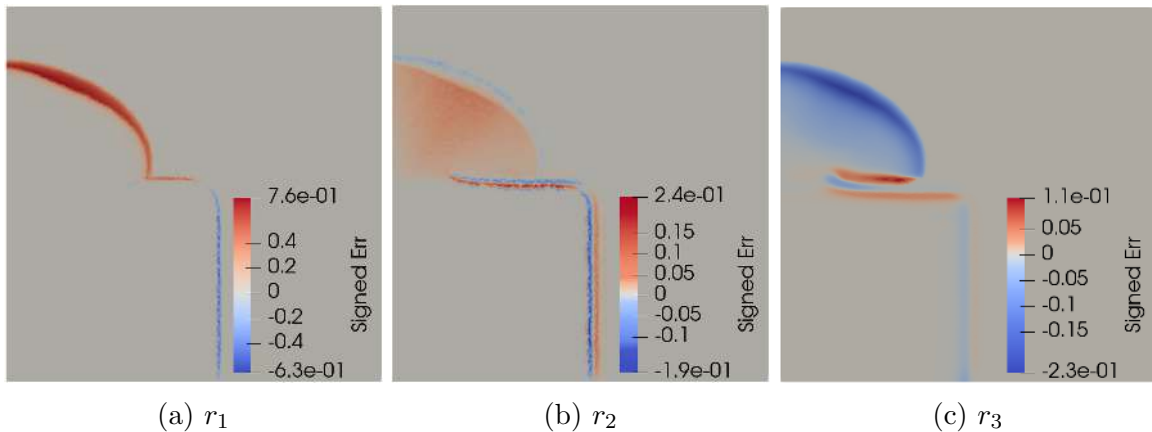(a) r_1 (b) r_2 (c) r_3

Figure 4.6: Differences in ionic quantities from varying SAD parameter D_2 at $t = 388\,\mathrm{ms}$. "Signed Err" is calculated as $x_0 - x_1$, where x_0 is the profile with $D_2 = 5.0\,\mathrm{e}-1$, and x_1 is the profile with $D_2 = 1.0\,\mathrm{e}-5$.

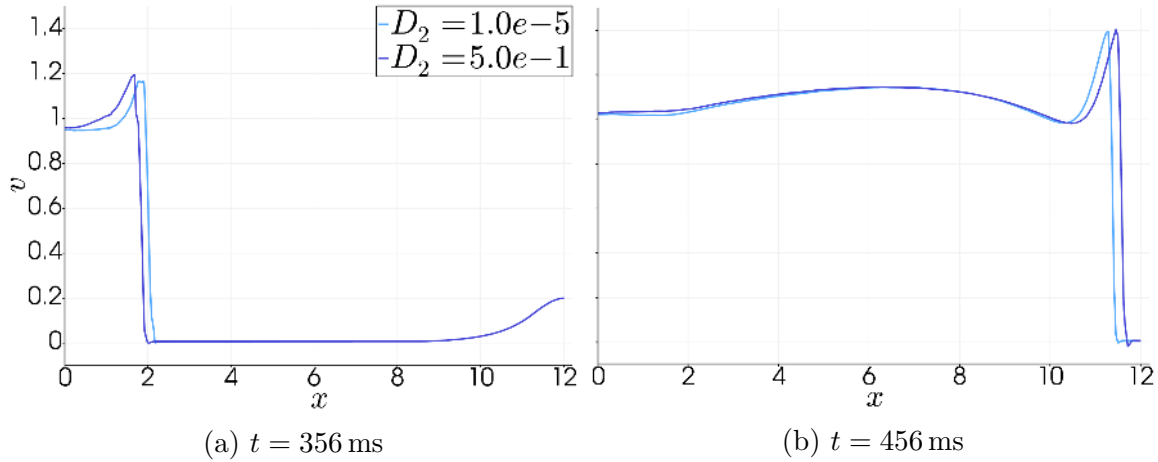(a) $t = 356$ ms   (b) $t = 456$ ms

Figure 4.7: Propagation of action potential with varying values of D_2. Propagation is measured by taking the profile of v over a horizontal line segment crossing the upper half of the tissue at $y = 7$ cm. The larger value of D_2 (dark blue) shows a higher conduction velocity.

It should be noted that conduction velocity was also sensitive to spatial discretization. This effect is documented in the literature [52]. In Table 4.3, we include the results of a simple convergence test for conduction velocity, similar to the benchmark test conducted in Rossi [53]. We calculated the horizontal propagation of the action potential using different timesteps and mesh refinements. We also conducted the analysis for $\Delta t = 0.6$ ms, but this timestep was too coarse to capture the kinetic dynamics, and thus the numerics did not converge. This test confirms that with
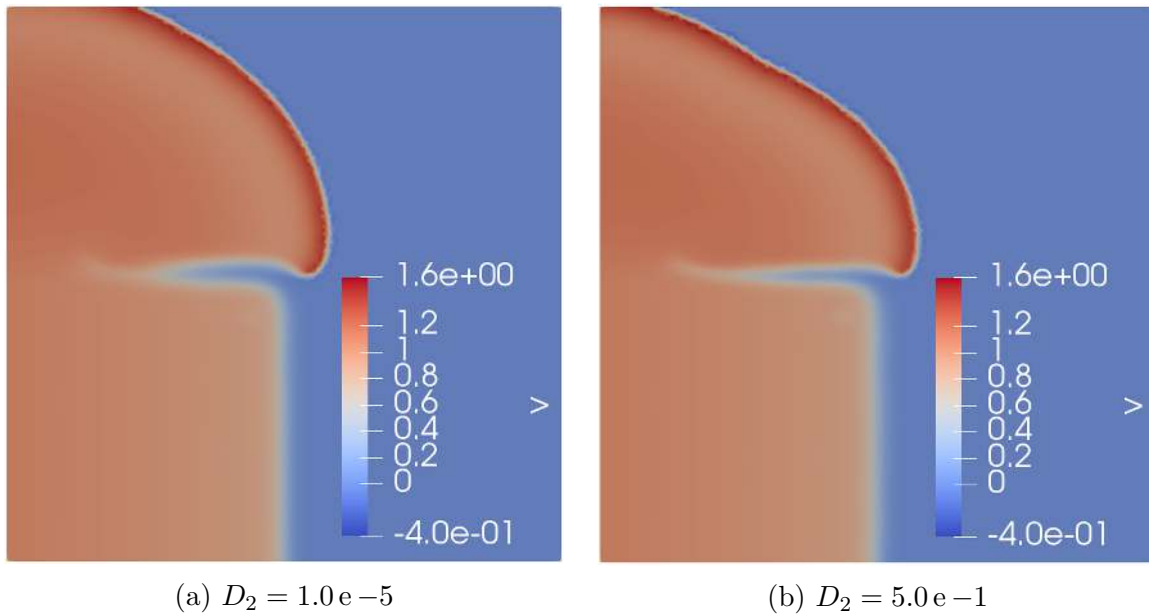

(a) $D_2 = 1.0\,e-5$ (b) $D_2 = 5.0\,e-1$

Figure 4.8: Effect of SAD on spiral wave at $t = 412$ ms in the viscoelastic case.

our timestep and mesh refinement (0.3 ms, and above $100,000$ DoF, respectively), conduction velocity is in the physiological range.

Convergence of Conduction Velocity, cm/ms				
DoF	h	$\Delta t = 0.05$ ms	$\Delta t = 0.1$ ms	$\Delta t = 0.3$ ms
27038	0.3817	0.2260	0.2063	0.2030
108576	0.1909	0.1569	0.1411	0.1368
170919	0.1527	0.1466	0.1315	0.1272
246456	0.1273	0.1401	0.1265	0.1200
554960	0.0849	0.1297	0.1161	0.1103

Table 4.3: Convergence of conduction velocity with respect to temporal and spatial discretization.

(a) $t = 340$ ms   (b) $t = 376$ ms   (c) $t = 416$ ms

(d) $t = 428$ ms   (e) $t = 456$ ms
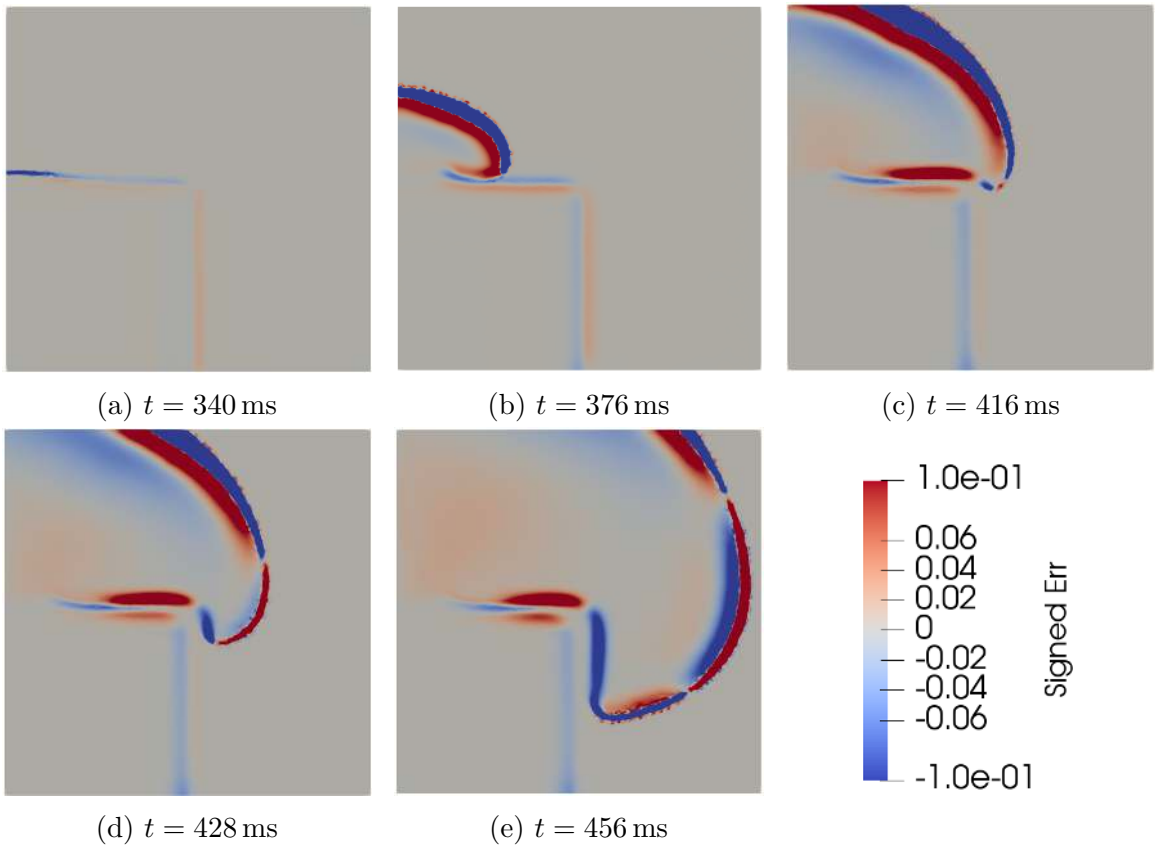
Figure 4.9: Voltage difference due to SAD, calculated as $v_A - v_B$, where A corresponds to $D_2 = 5.0\,\mathrm{e}-1$ and B corresponds to $D_2 = 1.0\,\mathrm{e}-5$. Note that the spiral develops earlier for the smaller value of D_2. However, after $t = 412$ ms, the spiral is more developed in the fiber direction (horizontally) with the larger value of D_2, indicating a faster conduction velocity in this direction.
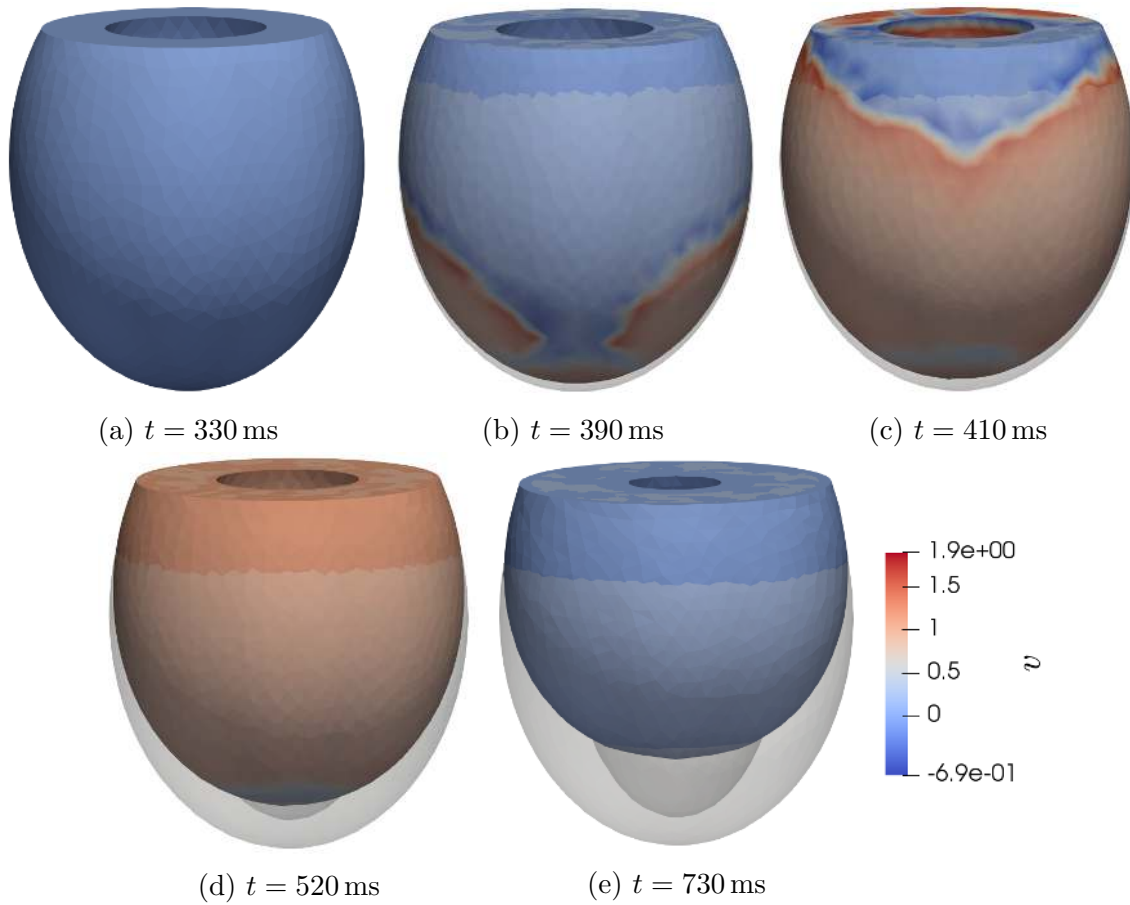
(a) $t = 330\,\text{ms}$ (b) $t = 390\,\text{ms}$ (c) $t = 410\,\text{ms}$

(d) $t = 520\,\text{ms}$ (e) $t = 730\,\text{ms}$

Figure 4.10: Evolution of voltage after S2 stimulus ($t = 335\,\text{ms}$), showing formation of a double-sided spiral wave on a contracting ventricle. The shadow of the original ventricle geometry is shown for comparison.

4.5   3D Results

We now review the results produced by implementing our model with the active strain formulation on an idealized 3D rendering of the left ventricle. After the S2 stimulus excites a group of cells in the lower left octant at $t = 335\,\text{ms}$, a spiral wave forms and sweeps around both sides of the ventricle, the two sides merging at approximately $t = 395\,\text{ms}$. Simultaneously, we see contraction in the upwards direction, complemented by torsion and thickening of the ventricle wall. Figure 4.10 shows the propagation of the action potential on the deforming ventricle, with the original ventricle geometry shown with reduced opacity for comparison. The S2 stimulus occurs on the underside of the ventricle and thus the nascent spiral is not visible in the images, but the two arms of the spiral can be seen later in Figure 4.10b.
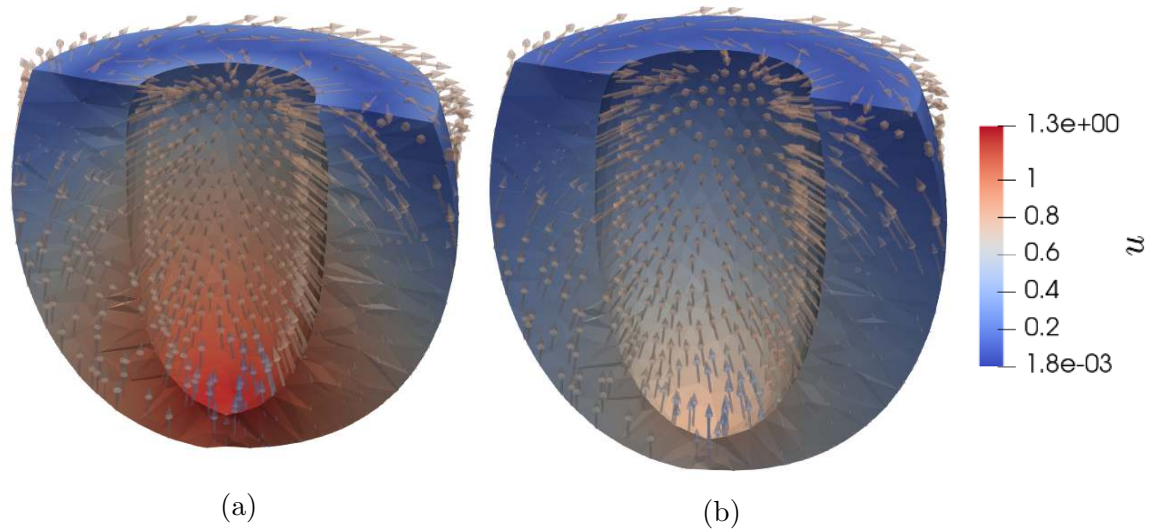
Figure 4.11: Comparison of displacement in hyperelastic and viscoelastic cases in 3D at $t = 560\,\mathrm{ms}$. Ventricle color represents magnitude of displacement, while arrows indicate displacement direction. The hyperelastic case (a) shows more contraction and wall-thickening than the viscoelastic case (b).

4.5.1 Effects of Viscosity

We found that the effects of viscosity in 3D were comparable to those seen in 2D. Figure 4.11 shows a comparison of the hyperelastic and viscoelastic case, with arrows pointing in the direction of displacement. The ventricle modeled as a hyperelastic tissue clearly undergoes more extreme displacement, contracting more overall and displaying greater wall thickening. This trend was consistent throughout the time interval evaluated (up to $1\,\mathrm{s}$). However, different from our 2D results, the pressure was not consistently greater in the hyperelastic case. Figure 4.12 shows the pressure profiles for both cases at $t = 550\,\mathrm{ms}$. In the hyperelastic case, pressure was concentrated on the inner boundary of the ventricular wall, decreasing rapidly in the outward direction. In the viscoelastic case, pressure was more evenly spread throughout the ventricular wall, showing a smoother profile than the hyperelastic case. As a result, pressure on the outer edge of the ventricular wall was higher in the viscoelastic case.

Conduction velocity was extremely similar between the hyperelastic and viscoelastic cases. The overall profiles of ionic quantities showed the same trends, as well. However, the voltage and calcium concentrations were generally higher in the viscoelastic case.
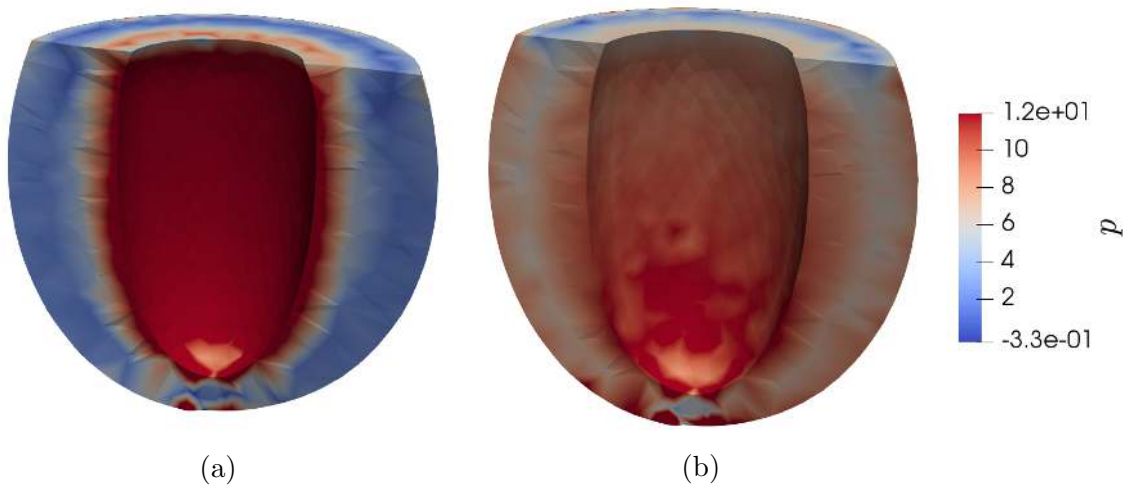
<div align="center">(a)   (b)</div>

Figure 4.12: Comparison of pressure in hyperelastic and viscoelastic cases in 3D at $t = 560\,\text{ms}$. Ventricle color represents pressure. The hyperelastic case (a) shows a high concentration of pressure in the endocardium (or inner ventricular wall), while the viscoelastic case (b) shows a smoother, more even distribution of pressure throughout the wall.

4.5.2   Stress-Assisted Diffusion

Similar to in the 2D case, SAD impacted the propagation of the spiral wave in a directionally dependent manner. In the fiber direction, SAD led to earlier advancement of the spiral. In the the transverse direction, the non-SAD case advanced earlier. Figure 4.13 shows the difference in voltage for the two cases (along with the actual voltage profile, for reference). The color contrast is indicative of a difference in the location of the peak voltage. The effect seen in the fiber direction (indicated by the white arrows in Figure 4.13) was not seen in the other directions. On the timescale by which the action potential moves through the ventricle, we were unable to detect a difference in conduction velocity. However, it is clear that there was a directionally-dependent effect of SAD on action potential propagation.

(a) $t = 382\,\mathrm{ms}$ (b) $t = 392\,\mathrm{ms}$
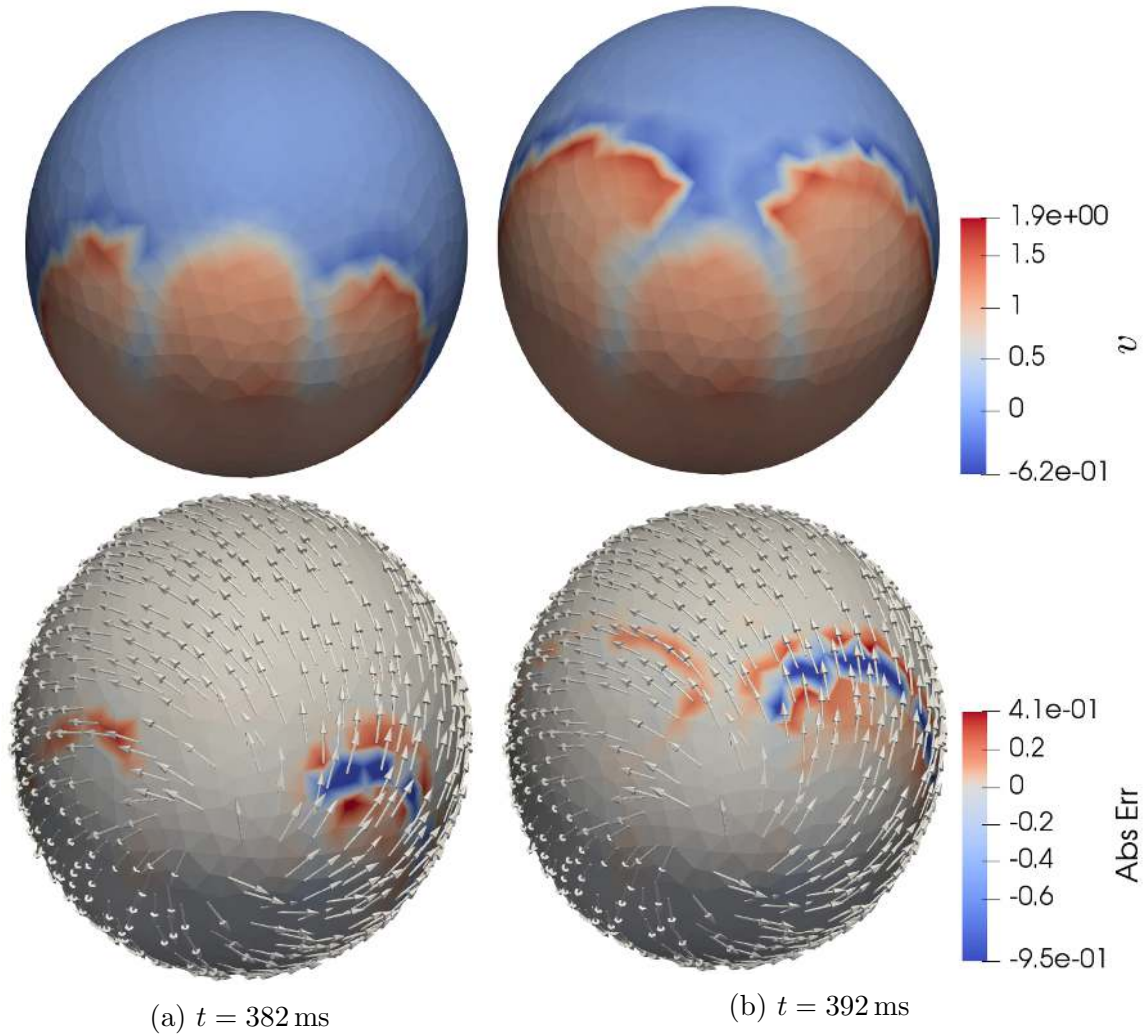
Figure 4.13: Effect of SAD on spiral wave propagation in 3D. These images are of the underside of the ventricle. The top panels show voltage, and the bottom panels show the difference between the SAD case and non-SAD case, calculated as $v_{\mathrm{SAD}} - v_{\mathrm{non\text{-}SAD}}$. The SAD case action potential propagated faster along the fiber direction than the non-SAD case action potential. The red on the outer edge of the spiral front indicates that the voltage peak, or the front of the action potential, was more advanced in the SAD case.

Chapter 5

Conclusions

In this dissertation, we modeled and numerically approximated the active contraction of the cardiac muscle. We focused particularly on the representation of the so-called mechanoelectrical feedback, incorporating a recent model of stress-assisted conductivity. Our model consists of a mechanical system, governed by nonlinear continuum mechanics, coupled with a four-variable minimal model for human ventricular action potential. We considered both the hyperelastic and viscoelastic cases, and both 2D and 3D domains. While we opted for an active stress formulation in 2D, due to convenience in calculating Π and avoidance of volumetric locking in the lowest-order case, we opted instead to adopt the active strain formulation in 3D. This allowed us to obtain a physiologically accurate deformation regime, although it required us to slightly reformulate our model.

Our work advances the field of cardiac electromechanics by incorporating several novel elements. Stress-assisted diffusion, in particular, is not often accounted for in such models. We combine this effect with an accurate model of human action potential, viscoelasticity, and a stress-based formulation in 2D. We also analyze the effect of SAD in 3D, which has not yet been done, although we do this for using an active-strain formulation.

In addition to evaluating the effects of certain model parameters and exploring the allowable range for D_2, we also detected robust effects of viscoelasticity and stress-assisted diffusion. Viscoelasticity consistently reduced the level of displacement and stress as the excitation wave passed through the tissue. It also resulted in more evenly distributed pressure throughout the tissue in 3D. These results are physically reasonable, as viscoelastic materials are known to dissipate energy as they deform [22].

Stress-assisted diffusion provided a directionally-dependent effect on action potential propagation. In 2D, SAD led to an increase in conduction velocity in the fiber

direction. In 3D, SAD resulted in an earlier development of the action potential in the fiber direction, though the ultimate effect on conduction velocity was unclear.

The nontrivial effects of both viscoelasticity and stress-assisted diffusion in our model suggest that they may play an important role in governing cardiac function and its response to external stimuli.However, further work remains in order to fully understand their contribution to the mechanical and electrophysiological behavior of cardiac tissue.

5.1   Extensions

The ultimate goal remains to create ever more realistic models of cardiac function. Further advancements to the theoretical framework built upon in this dissertation are readily apparent. Two non-invasive and natural extensions would be to run our model on physiologically detailed 3D geometries of the heart, and to validate our model against experimental results.

Perhaps the most pressing task motivated by this study, however, is further investigation of the discrepancies between the active stress and active strain formulations discussed in Section 2.2.1. We were unable to determine the reason for the stretching produced by the active stress formulation, in contrast to the contraction and wall-thickening in the active strain formulation. Preliminary experiments with different parameter values, formulations of active tension, and minor modifications to the active stress model were unsuccessful in producing the physiologically accurate deformation. Deeper analysis is thus required to bridge this gap.

Possible extensions to the model itself are numerous. The inclusion of temperature variations, for example, would simultaneously extend our model and that of Cherubini et al. [17]. A more physiologically accurate model should also consider poroelastic effects in order to account for perfusion of the tissue. We could additionally extend the minimal cell model and thermodynamically consistent activation model to state-of-the-art descriptions, which involve very large, stiff systems of ordinary differential equations. We could adopt the O'Hara et al. [47] model, involving 57 ODEs for ionic entities and currents, for example. Incorporating this type of model would require extensive testing of various operator splitting techniques and nonlinear solvers.

Another obvious next step would be to generalize our model to the use of bidomain equations instead of the monodomain model. Our current reaction-diffusion equation of the form

$$\chi \, \frac{\partial v}{\partial t} - \nabla \cdot (\mathbf{D} \, \nabla v) = I_{\text{ext}} - g(v, \vec{r}) \qquad\qquad \text{in } \Omega \times (0, t_{\text{final}}],$$

assumes equal anisotropy rates, meaning that the conductivity of the intracellular and extracellular domains are related by $\mathbf{D}_e = \lambda \mathbf{D}_i$, where λ is a constant scalar. Without this assumption, we would adopt a system of the form

$$\chi \frac{\partial v}{\partial t} - \nabla \cdot (\mathbf{D}_i \, \nabla v) - \nabla \cdot (\mathbf{D}_i \, \nabla u_e) = I_{\text{ext}} - g(v, \vec{r}) \qquad \text{in } \Omega \times (0, t_{\text{final}}],$$
$$-\nabla \cdot (\mathbf{D}_i \, \nabla v) - \nabla \cdot ((\mathbf{D}_i + \mathbf{D}_e) \, \nabla u_e) = 0 \qquad \text{in } \Omega \times (0, t_{\text{final}}],$$

which describes the transmembrane potential as the difference between intracellular and extracellular currents, $v = u_i - u_e$ [61]. This not only adds computational complexity, but requires careful consideration in modeling each conductivity tensor.

Taking this one step further, one could also investigate the appropriate transmission conditions to impose when considering a multi-domain environment, such as the heart-torso interface. Electromechanical coupling with the surrounding torso and organs would be a novel contribution to the field.

Appendix A

Model Parameters

Mechanical Parameters					
a	0.23621	[N/cm^2]	b	10.810	[$-$]
a_f	0.116037	[N/cm^2]	b_f	14.154	[$-$]
a_s	0.37245	[N/cm^2]	b_s	5.1645	[$-$]
a_{fs}	4.0108	[N/cm^2]	b_{fs}	11.300	[$-$]
η	0.01	[N/cm^2]	p_N	0.1	[$-$]
η_a	0.001	[N/cm^2]	η_b	0.01	[N/cm^2]
β	0.01	[s]	γ	22.6	[Pa$\cdot$s]

Table A.1: Mechanical model parameters.

Electrochemical Parameters			
v_o	0.0	$\tau_{1,1}^-$	60.0
v_v	1.55	$\tau_{1,2}^-$	1150.0
v_2^-	0.03	$\tau_{2,1}^-$	60.0
v_{so}	0.65	$\tau_{2,2}^-$	15.0
v_3	0.9087	τ_{so}	0.11
θ_1	0.3	τ_{o1}	30.0181
θ_1^-	0.006	τ_{o2}	0.9957
θ_2	0.13	$\tau_{\mathrm{so},1}$	2.0458
θ_o	0.006	$\tau_{\mathrm{so},2}$	0.65
k_2^-	65.0	$\tau_{3,1}$	2.7342
k_3	2.0994	$\tau_{3,2}$	16.0
k_{so}	2.0458	τ_{so}	1.8875
$r_{1,\infty}^*$	0.94	τ_1^+	1.4506
$\tau_{2,\infty}$	0.07	τ_2^+	200.0

Table A.2: Monodomain equation parameters. All parameters are dimensionless.

Coupling Parameters					
D_0	1.171	[cm^2/s]	α_1	10.0	[$-$]
D_1	0.9	[cm^2/s]	α_2	0.5	[$-$]
D_2	0.01	[cm^2/s]			

Table A.3: Parameters governing electromechanical coupling.

Bibliography

[1] Cardiovascular diseases (cvds). Technical report, World Health Organization, May 2017. URL `http://www.who.int/en/news-room/fact-sheets/detail/cardiovascular-diseases-(cvds)`. Date Accessed: 02 August 2018.

[2] M. S. Alnæs, J. Blechta, J. Hake, A. Johansson, B. Kehlet, A. Logg, C. Richardson, J. Ring, M. E. Rognes, and G. N. Wells. The fenics project version 1.5. *Archive of Numerical Software*, 3(100):9–23, 2015.

[3] D. Ambrosi and S. Pezzuto. Active stress vs. active strain in mechanobiology: constitutive issues. *Journal of Elasticity*, 107(2):199–212, 2012.

[4] B. Andreianov, M. Bendahmane, A. Quarteroni, and R. Ruiz Baier. Solvability analysis and numerical approximation of linearized cardiac electromechanics. *Mathematical Models and Methods in Applied Sciences*, 25(05):959–993, 2015.

[5] C. M. Augustin, A. Neic, M. Liebmann, A. J. Prassl, S. A. Niederer, G. Haase, and G. Plank. Anatomically accurate high resolution modeling of human whole heart electromechanics: a strongly scalable algebraic multigrid solver method for nonlinear deformation. *Journal of Computational Physics*, 305:622–646, 2016.

[6] L. Barbarotta, S. Rossi, L. Dede, and A. Quarteroni. A transmurally heterogeneous orthotropic activation model for ventricular contraction and its numerical validation. *International Journal for Numerical Methods in Biomedical Engineering*, 2017. URL `https://www.mate.polimi.it/biblioteca/add/qmox/62-2017.pdf`.

[7] D. Baroli, A. Quarteroni, and R. Ruiz Baier. Convergence of a stabilized discontinuous galerkin method for incompressible nonlinear elasticity. *Advances in Computational Mathematics*, 39(2):425–443, 2013.

[8] D. H. Birnie and A. S. Tang. The problem of non-response to cardiac resynchronization therapy. *Current Opinion in Cardiology*, 21(1):20–26, 2006.

[9] Y. Bourgault and C. Pierre. Comparing the bidomain and monodomain models in electro-cardiology through convergence analysis. 2010. URL `https://hal.archives-ouvertes.fr/hal-00545888/file/PRB1_janv2011.pdf`.

[10] A. Bueno-Orovio, E. M. Cherry, and F. H. Fenton. Minimal model for human ventricular action potentials in tissue. *Journal of Theoretical Biology*, 253(3): 544–560, 2008.

[11] R. Bürger, P. E. Mendez, and R. Ruiz Baier. On h(div)-conforming methods for double-diffusion equations in porous media. *preprint*, 2018. URL `ftp://ftp.ci2ma.udec.cl/pub/ci2ma/pre-publicaciones/2018/pp18-30.pdf`.

[12] E. Burman and M. A. Fernández. Galerkin finite element methods with symmetric pressure stabilization for the transient stokes equations: stability and convergence analysis. *SIAM Journal on Numerical Analysis*, 47(1):409–439, 2008.

[13] R. Chabiniok, V. Y. Wang, M. Hadjicharalambous, L. Asner, J. Lee, M. Sermesant, E. Kuhl, A. A. Young, P. Moireau, M. P. Nash, et al. Multiphysics and multiscale modelling, data–model fusion and integration of organ physiology in the clinic: ventricular cardiac mechanics. *Interface Focus*, 6(2):20150083, 2016.

[14] K. Chavan, B. P. Lamichhane, and B. I. Wohlmuth. Locking-free finite element methods for linear and nonlinear elasticity in 2d and 3d. *Computer Methods in Applied Mechanics and Engineering*, 196:4075–4086, 2007.

[15] J. Chen, W. Liu, H. Zhang, L. Lacy, X. Yang, S.-K. Song, S. A. Wickline, and X. Yu. Regional ventricular wall thickening reflects changes in cardiac fiber and sheet structure during contraction: quantification with diffusion tensor mri. *American Journal of Physiology-Heart and Circulatory Physiology*, 289(5): H1898–H1907, 2005.

[16] C. Cherubini, S. Filippi, A. Gizzi, and R. Ruiz Baier. A note on stress-driven anisotropic diffusion and its role in active deformable media. *Journal of Theoretical Biology*, 430:221–228, 2017.

[17] C. Cherubini, S. Filippi, A. Gizzi, A. Loppini, and R. Ruiz Baier. Thermo-electric effects in an anisotropic active strain electromechanical model. *arXiv preprint arXiv:1805.00757*, 2018.

[18] J. Christoph, M. Chebbok, C. Richter, J. Schröder-Schetelig, P. Bittihn, S. Stein, I. Uzelac, F. Fenton, G. Hasenfuß, R. Gilmour Jr, et al. Electromechanical vortex filaments during cardiac fibrillation. *Nature*, 555(7698):667, 2018.

[19] P. Colli Franzone, L. F. Pavarino, and S. Scacchi. Bioelectrical effects of mechanical feedbacks in a strongly coupled cardiac electro-mechanical model. *Mathematical Models and Methods in Applied Sciences*, 26(01):27–57, 2016.

[20] F. S. Costabal, F. A. Concha, D. E. Hurtado, and E. Kuhl. The importance of mechano-electrical feedback and inertia in cardiac electromechanics. *Computer Methods in Applied Mechanics and Engineering*, 320:352–368, 2017.

[21] F. Fenton and A. Karma. Vortex dynamics in three-dimensional continuous myocardium with fiber rotation: Filament instability and fibrillation. *Chaos: An Interdisciplinary Journal of Nonlinear Science*, 8(1):20–47, 1998.

[22] H. Y. Gan and Y. C. Lam. *Viscoelasticity*, pages 1–12. Springer US, Boston, MA, 2013. ISBN 978-3-642-27758-0. doi: 10.1007/978-3-642-27758-0_1666-2. URL `https://doi.org/10.1007/978-3-642-27758-0_1666-2`.

[23] G. N. Gatica. A simple introduction to the mixed finite element method. *Theory and Applications. Springer Briefs in Mathematics. Springer, London*, 2014.

[24] G. N. Gatica, B. Gomez-Vargas, and R. Ruiz Baier. Analysis and mixed-primal finite element discretisations for stress-assisted diffusion problems. *Comput. Methods Appl. Mech. Engrg.*, 337:411–438, 2018. doi: 10.1016/j.cma.2018.03.043. URL `./myPapers/ggr_cmame18.pdf`.

[25] C. Geuzaine and J.-F. Remacle. Gmsh: A three-dimensional finite element mesh generator with built-in pre- and post-processing facilities. *International Journal for Numerical Methods in Engineering*, 79(11):1309–1331, 2009.

[26] S. Göktepe, S. Acharya, J. Wong, and E. Kuhl. Computational modeling of passive myocardium. *International Journal for Numerical Methods in Biomedical Engineering*, 27(1):1–12, 2011.

[27] V. Gurev, T. Lee, J. Constantino, H. Arevalo, and N. A. Trayanova. Models of cardiac electromechanics based on individual hearts imaging data. *Biomechanics and Modeling in Mechanobiology*, 10(3):295–306, 2011.

[28] M. Hadjicharalambous, J. Lee, N. P. Smith, and D. A. Nordsletten. A displacement-based finite element formulation for incompressible and nearly-incompressible cardiac mechanics. *Computer Methods in Applied Mechanics and Engineering*, 274:213–236, 2014.

[29] G. A. Holzapfel. *Nonlinear solid mechanics: A continuum approach for engineering.* John Wiley and Sons. Ltd, 2000.

[30] G. A. Holzapfel and R. W. Ogden. Constitutive modelling of passive myocardium: a structurally based framework for material characterization. *Philosophical Transactions of the Royal Society of London A: Mathematical, Physical and Engineering Sciences*, 367(1902):3445–3475, 2009.

[31] V. Iyer, R. Mazhari, and R. L. Winslow. A computational model of the human left-ventricular epicardial myocyte. *Biophysical Journal*, 87(3):1507–1525, 2004.

[32] L. M. Jaffe and D. P. Morin. Cardiac resynchronization therapy: history, present status, and future directions. *The Ochsner Journal*, 14(4):596–607, 2014.

[33] K. S. Karlsen. Effects of inertia in modeling of left ventricular mechanics. Master's thesis, University of Oslo, 2017.

[34] A. Karma. Spiral breakup in model equations of action potential propagation in cardiac tissue. *Physical Review Letters*, 71(7):1103, 1993.

[35] A. Karma. Physics of cardiac arrhythmogenesis. *Annual Review of Condensed Matter Physics*, 4(1):313–337, 2013.

[36] R. Keldermann, M. Nash, and A. Panfilov. Modeling cardiac mechano-electrical feedback using reaction-diffusion-mechanics systems. *Physica D: Nonlinear Phenomena*, 238(11-12):1000–1007, 2009.

[37] P. Kohl, P. Hunter, and D. Noble. Stretch-induced changes in heart rate and rhythm: clinical observations, experiments and mathematical models. *Progress in Biophysics and Molecular Biology*, 71(1):91–138, 1999.

[38] V. Kumaran. *Rheology of Complex Fluids*, chapter 2: Fundamentals of Rheology. Springer, 2010.

[39] B. P. Lamichhane and E. P. Stephan. A symmetric mixed finite element method for nearly incompressible elasticity based on biorthogonal systems. *Numerical Methods for Partial Differential Equations*, 28(4):1336–1353, 2012.

[40] S. Land, S.-J. Park-Holohan, N. P. Smith, C. G. dos Remedios, J. C. Kentish, and S. A. Niederer. A model of cardiac contraction based on novel measurements of tension development in human cardiomyocytes. *Journal of Molecular and Cellular Cardiology*, 106:68–83, 2017.

[41] A. Lopez-Perez, R. Sebastian, and J. M. Ferrero. Three-dimensional cardiac computational modelling: methods, features and applications. *Biomedical Engineering Online*, 14(1):35, 2015.

[42] A. Loppini, A. Gizzi, R. Ruiz Baier, C. Cherubini, F. Fenton, and S. Filippi. Competing mechanisms of stress-assisted diffusivity and stretch-activated currents in cardiac electromechanics. *arXiv preprint arXiv:1805.00768*, 2018.

[43] C. Lu, W. Huang, and J. Qiu. Maximum principle in linear finite element approximations of anisotropic diffusion–convection–reaction problems. *Numerische Mathematik*, 127(3):515–537, 2014.

[44] A. Minajeva, M. Kulke, J. M. Fernandez, and W. A. Linke. Unfolding of titin domains explains the viscoelastic behavior of skeletal myofibrils. *Biophysical Journal*, 80(3):1442–1451, 2001.

[45] M. P. Nash and A. V. Panfilov. Electromechanical model of excitable tissue to study reentrant cardiac arrhythmias. *Progress in Biophysics and Molecular Biology*, 85(2-3):501–522, 2004.

[46] S. Norburn and D. Silvester. Stabilised vs. stable mixed methods for incompressible flow. *Computer Methods in Applied Mechanics and Engineering*, 166(1-2): 131–141, 1998.

[47] T. O'Hara, L. Virág, A. Varró, and Y. Rudy. Simulation of the undiseased human cardiac ventricular action potential: model formulation and experimental validation. *PLoS Computational Biology*, 7(5):e1002061, 2011.

[48] M. Orini, A. Nanda, M. Yates, C. Di Salvo, N. Roberts, P. Lambiase, and P. Taggart. Mechano-electrical feedback in the clinical setting: Current perspectives. *Progress in Biophysics and Molecular Biology*, 130:365–375, 2017.

[49] S. Pezzuto, D. Ambrosi, and A. Quarteroni. An orthotropic active–strain model for the myocardium mechanics and its numerical approximation. *European Journal of Mechanics-A/Solids*, 48:83–96, 2014.

[50] J. D. Pollock and A. N. Makaryus. Physiology, cardiovascular, cardiac cycle. 2018. URL `https://www.ncbi.nlm.nih.gov/books/NBK459327/`.

[51] M. Potse, B. Dubé, J. Richer, A. Vinet, and R. M. Gulrajani. A comparison of monodomain and bidomain reaction-diffusion models for action potential propagation in the human heart. *IEEE Transactions on Biomedical Engineering*, 53 (12):2425–2435, 2006.

[52] A. Quarteroni, T. Lassila, S. Rossi, and R. Ruiz Baier. Integrated heart—coupling multiscale and multiphysics models for the simulation of the cardiac function. *Computer Methods in Applied Mechanics and Engineering*, 314:345–407, 2017.

[53] S. Rossi. *Anisotropic Modeling of Cardiac Mechanical Activation*. PhD thesis, Ecole Polytechnique Fédérale de Lausanne, 2014. Co-supervision with: Instituto Superior Técnico (IST) da Universidade [Técnica] de Lisboa, Centro de Matemática e Aplicações, Doutoramento em Matemática.

[54] S. Rossi, R. Ruiz Baier, L. F. Pavarino, and A. Quarteroni. Orthotropic active strain models for the numerical simulation of cardiac biomechanics. *International Journal for Numerical Methods in Biomedical Engineering*, 28(6-7): 761–788, 2012.

[55] S. Rossi, T. Lassila, R. Ruiz Baier, A. Sequeira, and A. Quarteroni. Thermodynamically consistent orthotropic activation model capturing ventricular systolic wall thickening in cardiac electromechanics. *European Journal of Mechanics-A/Solids*, 48:129–142, 2014.

[56] R. Ruiz Baier. Primal-mixed formulations for reaction–diffusion systems on deforming domains. *Journal of Computational Physics*, 299:320–338, 2015.

[57] G. Scovazzi, B. Carnes, X. Zeng, and S. Rossi. A simple, stable, and accurate linear tetrahedral finite element for transient, nearly, and fully incompressible solid dynamics: a dynamic variational multiscale approach. *International Journal for Numerical Methods in Engineering*, 106(10):799–839, 2016.

[58] P. P. Sengupta, J. Korinek, M. Belohlavek, J. Narula, M. A. Vannan, A. Jahangir, and B. K. Khandheria. Left ventricular structure and function: basic science for cardiac imaging. *Journal of the American College of Cardiology*, 48(10):1988–2001, 2006.

[59] G. Sommer, A. J. Schriefl, M. Andrä, M. Sacherer, C. Viertler, H. Wolinski, and G. A. Holzapfel. Biomechanical properties and microstructure of human ventricular myocardium. *Acta Biomaterialia*, 24:172–192, 2015.

[60] R. W. Soutas-Little. *Elasticity*. Courier Corporation, 1999.

[61] J. Sundnes, G. T. Lines, X. Cai, B. F. Nielsen, K.-A. Mardal, and A. Tveito. *Computing the electrical activity in the heart*, volume 1. Springer Science & Business Media, 2007.

[62] J. Sundnes, S. Wall, H. Osnes, T. Thorvaldsen, and A. D. McCulloch. Improved discretisation and linearisation of active tension in strongly coupled cardiac electro-mechanics simulations. *Computer Methods in Biomechanics and Biomedical Engineering*, 17(6):604–615, 2014.

[63] K. Ten Tusscher, D. Noble, P.-J. Noble, and A. V. Panfilov. A model for human ventricular tissue. *American Journal of Physiology-Heart and Circulatory Physiology*, 286(4):H1573–H1589, 2004.

[64] N. A. Trayanova. Whole-heart modeling: applications to cardiac electrophysiology and electromechanics. *Circulation Research*, 108(1):113–128, 2011.

[65] N. A. Trayanova, J. Constantino, and V. Gurev. Models of stretch-activated ventricular arrhythmias. *Journal of Electrocardiology*, 43(6):479–485, 2010.

[66] T. Usyk, R. Mazhari, and A. McCulloch. Effect of laminar orthotropic myofiber architecture on regional stress and strain in the canine left ventricle. *Journal of Elasticity and the Physical Science of Solids*, 61(1-3):143–164, 2000.

[67] E. J. Vigmond, C. Clements, D. M. McQueen, and C. S. Peskin. Effect of bundle branch block on cardiac output: a whole heart simulation study. *Progress in Biophysics and Molecular Biology*, 97(2-3):520–542, 2008.

[68] H. Watanabe, S. Sugiura, H. Kafuku, and T. Hisada. Multiphysics simulation of left ventricular filling dynamics using fluid-structure interaction finite element method. *Biophysical Journal*, 87(3):2074–2085, 2004.

[69] D. P. Zipes. Proarrhythmic effects of antiarrhythmic drugs. *American Journal of Cardiology*, 59(11):E26–E31, 1987.